Journal of the Mechanics and Physics of Solids 106 (2017) 229–256

Contents lists available at ScienceDirect

Journal of the Mechanics and Physics of Solids

journal homepage: www.elsevier.com/locate/jmps

Instabilities in confined elastic layers under tension: Fringe, fingering and cavitation

Shaoting Lin[a,1], Yunwei Mao[a,1], Raul Radovitzky[b], Xuanhe Zhao[a,c,*]

[a] Department of Mechanical Engineering, Massachusetts Institute of Technology, Cambridge, MA 02139, USA
[b] Department of Aeronautics and Astronautics, Massachusetts Institute of Technology, Cambridge, MA 02139, USA
[c] Department of Civil and Environmental Engineering, Massachusetts Institute of Technology, Cambridge, MA 02139, USA

ARTICLE INFO

Article history:
Received 12 April 2017
Revised 18 May 2017
Accepted 18 May 2017
Available online 23 May 2017

Keywords:
Fringe instability
Fingering instability
Adhesion
Cavitation
Confined layers

ABSTRACT

Under tension, confined elastic layers can exhibit various modes of mechanical instabilities, including cavitation, fingering and fringe instabilities. While the cavitation has been extensively studied, the fingering and fringe instabilities have not been well understood, and the relations and interactions of these instabilities have not been explored yet. In this paper, we systematically study the formation, transition, interaction and co-existence of mechanical instabilities in confined elastic layers under tension. Through combined experimental, numerical and theoretical analysis, we find that the mode of instability is determined by both geometry and mechanical properties of the elastic layer through two non-dimensional parameters: layer's lateral dimension over its thickness and elastocapillary length over the defect size. A phase diagram is calculated to quantitatively predict the occurrence of any mode of instability. We further show cavitation instability and fingering instability can co-exist and interact with each other in one elastic layer. The current work can help the design of robust adhesives by rationally harnessing the desired mode of instabilities while suppressing the other modes.

1. Introduction

Elastic layers with top and bottom surfaces adhered to rigid bodies are abundant in biological organisms such as mussel plaques on rocks (Waite et al., 2005), barnacle glues on ship hulks (Vaccaro and Waite, 2001) and tendons on bones (Benjamin et al., 2006; Desmond et al., 2015). In addition to the examples in nature, the stressed elastic layers have been widely adopted in engineering applications such as sealants, insulators, bearings, and adhesives (Biggins et al., 2013; Creton and Ciccotti, 2016; Shull, 2002). More recently, tough and soft hydrogel adhesives (Casares et al., 2015; Cha et al., 2013; Rose et al., 2014; Yuk et al., 2016a) have also been used in biocompatible soft robotics (Kim et al., 2015; Palleau et al., 2013; Yuk et al., 2017), electronics (Keplinger et al., 2013; Lin et al., 2016) and living devices (Lind et al., 2017; Liu et al., 2017).

When the rigid bodies are pulled apart, the stressed elastic layers can undergo various modes of mechanical instabilities due to mechanical loads and constraints. The formation and interaction of these mechanical instabilities highly affect the mechanical robustness of engineering structures. For example, the load capacity of the adhesives highly depends on the

---

* Corresponding author at: Department of Mechanical Engineering, Massachusetts Institute of Technology, Cambridge, MA 02139, USA.
E-mail address: zhaox@mit.edu (X. Zhao).

[1] These authors contributed equally to this work.

http://dx.doi.org/10.1016/j.jmps.2017.05.011
0022-5096/© 2017 Elsevier Ltd. All rights reserved.

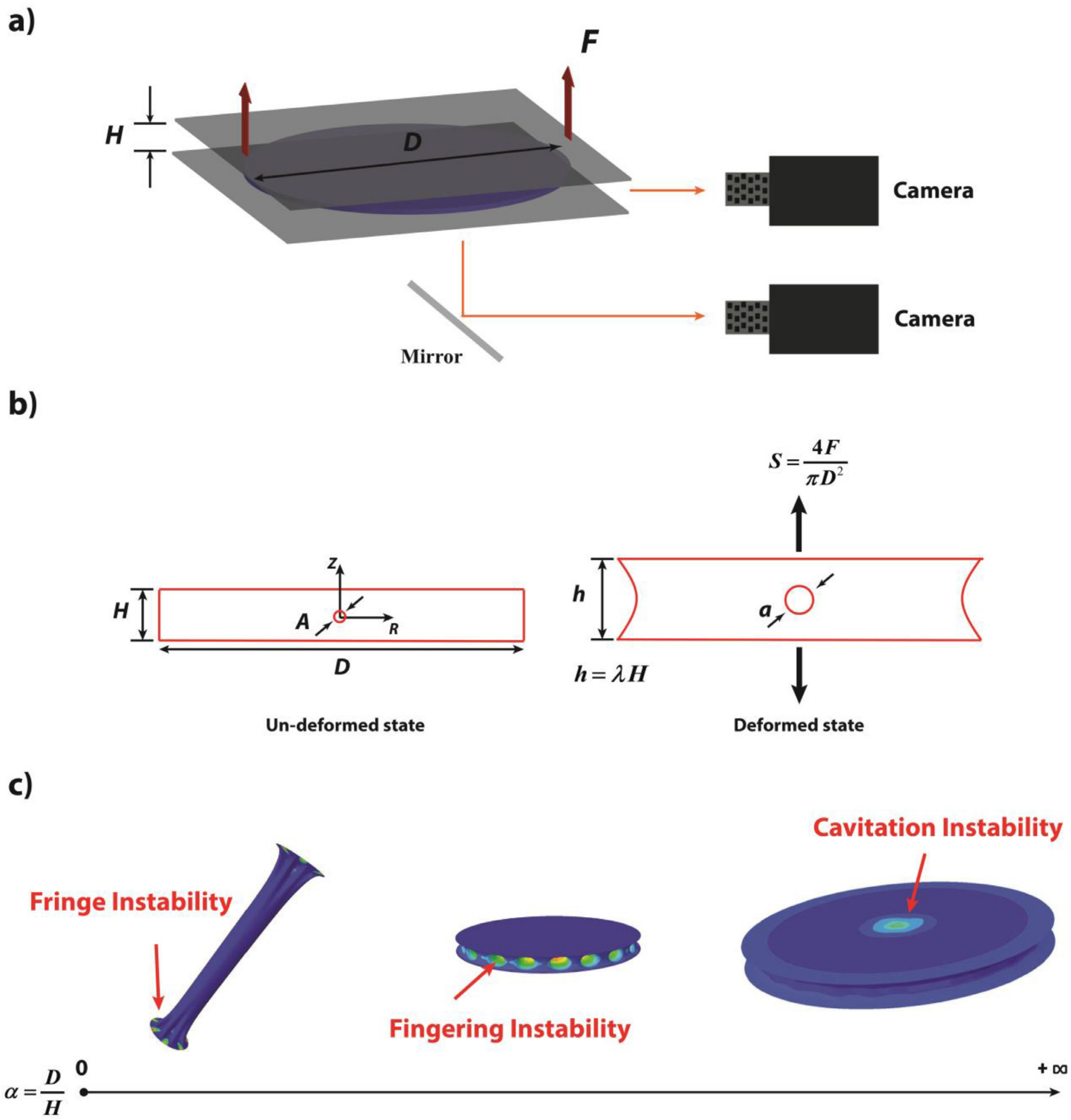

Fig. 1. Schematics on deformation and instabilities in confined elastics layers under tension. a) Experimental setup. b) The cross-section of the constrained elastic layer in un-deformed and deformed state. c) Illustration of fringe instability, fingering instability and cavitation instability, corresponding to small, moderate and large aspect ratio $\alpha = D/H$, respectively.

occurrence of mechanical instabilities (Creton and Ciccotti, 2016). The emergence of mechanical instabilities can also initiate different failure mechanisms ranging from interfacial fracture to cohesive failure in relevant structures (Crosby et al., 2000).

In recent decades, various modes of mechanical instabilities in confined elastic layers under tension have been discovered (Biggins et al., 2013; Gent and Lindley, 1959b; Ghatak and Chaudhury, 2003; Lin et al., 2016; Shull et al., 2000). If the elastic layer partially debonds from the rigid body, the delaminated interface can undulate periodically to give the interfacial undulation (Chakrabarti and Chaudhury, 2013; Chaudhury et al., 2015; Chung et al., 2006; Chung and Chaudhury, 2005; Ghatak and Chaudhury, 2003). If perfect bonding between the elastic layer and the rigid bodies is maintained, a cavity can nucleate and grow within the elastic layer when the hydrostatic tensile stress in any region of the elastic layer reaches a critical value, giving the cavitation instability (e.g., Fig. 1c) (Ball, 1982; Fond, 2001; Gent and Lindley, 1959b; Hang-Sheng and Abeyaratne, 1992; Lopez-Pamies et al., 2011). Even if perfect bonding between the elastic layer and the rigid substrates is maintained and cavitation instability is suppressed by tuning the material properties and geometry of the elastic layer, the exposed meniscus can become unstable, forming fingering instability (Biggins et al., 2013; Overvelde et al., 2016; Shull et al., 2000) or fringe instability (Lin et al., 2016). While fingering instability initiates at the middle section of the exposed meniscus, fringe instability forms at the fringe portion of the exposed meniscus (e.g., Fig. 1).

This paper is aimed to provide a systematic understanding on the relations and interactions of the three modes of instabilities in perfectly-bonded elastic layers under tension: cavitation, fingering and fringe instabilities. While the cavitation instability has been intensively studied (Gent and Lindley, 1959b; Kundu and Crosby, 2009), the recently-discovered fingering and fringe instabilities have not been well understood (Biggins et al., 2013; Shull et al., 2000). It is known that the instability is determined by the geometries and mechanical properties of the elastic layers, but there exists no model or theory to predict which mode (i.e., cavitation, fingering or fringe) will emerge in perfectly-bonded elastic layers under tension. In addition, the co-existence and interactions of different modes of instabilities have not been studied.

In this paper, we perform the first set of systematic study on the formation, transition, interaction and co-existence of mechanical instabilities in confined elastic layers under tension, through combined experimental, numerical and theoretical analysis. We first discuss the characteristic features of individual mode of instability. Then we develop a theory for large deformation in a confined elastic layer with cylindrical shape under tension. The theory can correlate the applied stress, the applied stretch and the hydrostatic pressure in the elastic layer. Thereafter, we perform the linear perturbation analysis on the deformation of the elastic layer to theoretically predict the onset of fringe and fingering instabilities; and theoretically calculate the critical stress and critical stretch of cavitation instability. We find that the initial occurrence of instability can be tuned by both geometrical and mechanical properties of the elastic layer through two non-dimensional parameters: layer's lateral dimension over its thickness and elastocapillary length over the defect size. We further show that cavitation instability and fingering instability can coexist in one elastic layer under tension. Systematically understanding of the formation and interactions of various mechanical instabilities in elastic layers under tension can provide a guideline for the design of robust adhesives by rationally harnessing the desired mode of instabilities while suppressing the other modes.

The plan of the paper is as follow. Section 2 defines the physical and dimensionless parameters used in this work. In Section 3, we discuss the experimental and simulation methods. In Section 4, we qualitatively discuss various modes of instabilities in elastic layers under tension. In Section 5, we first derive the deformation field in constrained elastic layer under tension, and then identify the critical point for the onset of each mode of instability using perturbation theory. In Section 6, we discuss the formation and evolution of each mode of instability through combined experimental and simulation results. We particularly discuss the relations between the applied stress and stretch in elastic layers under tension. In Section 7, we construct a phase diagram to predict the occurrence of any mode of instability in elastic layers. In Section 8, we discuss the coexistence and interactions of cavitation instability and fingering instability in one elastic layer under tension.

2. Physical and dimensionless parameters

As illustrated on Fig. 1b, we focus on elastic layers of cylindrical shape with height H and diameter D at the un-deformed (reference) state in this work. The material of the elastic layer is taken to be neo-Hookean with shear modulus μ and surface energy γ. Cavities with maximum diameter A may exist in the layer as defects. A ratio between surface energy and shear modulus of the material, γ/μ, gives the elastocapillary length, which characterizes the effect of the surface tension on the mechanical behaviors of the material. In the current study, we set the elastocapillary length γ/μ to be much smaller than the macroscopic dimensions of the sample (i.e. H and D), but on the same order or larger than the defect size A. Through dimensional argument, we can obtain the following two dimensionless parameters:

$$\alpha = \frac{D}{H}, \quad \beta = \frac{\gamma}{\mu A}, \tag{1}$$

which affect the mechanical behavior of the elastic layer. The elastic layer is bonded on two rigid plates without delamination during its deformation and instabilities. A tensile force F is applied on the rigid plates, which deforms the elastic layer to the current height h. We define the applied nominal stress S and the applied stretch λ on the elastic layer as (see Fig. 1)

$$S = \frac{4F}{\pi D^2}, \quad \lambda = \frac{h}{H}. \tag{2}$$

When the applied nominal stress or stretch reaches a critical value S_c or λ_c, a mode of instability sets in the elastic layer.

Geometrically, the cylindrical elastic layer in the un-deformed state occupies a region $0 \le R \le D/2$, $0 \le \Theta < 2\pi$ and $-H/2 \le Z \le H/2$. For convenience, we define the normalized location at the reference configuration $\bar{R} = \frac{R}{D/2}$ and $\bar{Z} = \frac{Z}{H/2}$ with $\bar{R} \in [0, 1]$ and $\bar{Z} \in [-1, 1]$.

3. Experimental and simulation methods

3.1. Sample preparation

We chose polyacrylamide hydrogel (PAAm) as a model hyper-elastic solid with negligible hysteresis and low rate sensitivity (Lin et al., 2016; Lin et al., 2014b; Mao et al., 2017; Yang et al., 2013). To make a PAAm hydrogel sample, a precursor

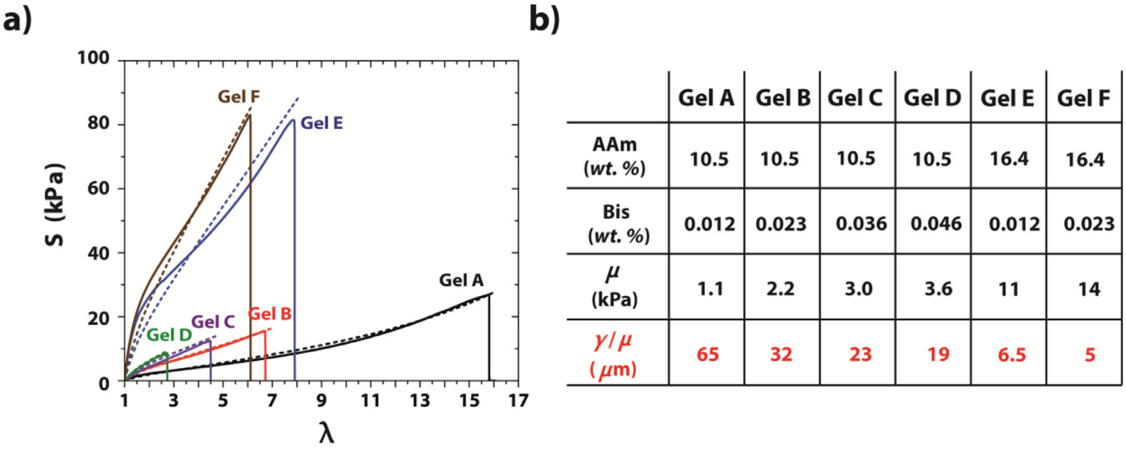

	Gel A	Gel B	Gel C	Gel D	Gel E	Gel F
AAm (*wt.* %)	10.5	10.5	10.5	10.5	16.4	16.4
Bis (*wt.* %)	0.012	0.023	0.036	0.046	0.012	0.023
μ (kPa)	1.1	2.2	3.0	3.6	11	14
γ/μ (μm)	65	32	23	19	6.5	5

Fig. 2. Materials for the constrained elastic layers. a) Measured nominal stress–stretch curves for the samples with various constituents. Solid line represents the experimental data; dashed line represents the fitted neo-Hookean model. b) Weight ratio of polyacrylamide (AAm) and N,N′-methylenebisacrylamide (Bis), shear modulus $\mu$and elastocapillary length γ/μ for each material.

solution was prepared by mixing acrylamide (Sigma, A8887), alginate (Sigma, A2033), N,N-methylenebisacrylamide (Sigma, 146072) as the crosslinker for polyacrylamide and 102 µl 0.2 M ammonium persulfate (Sigma, 248614) as an initiator for polyacrylamide (Lin et al., 2014a; Lin et al., 2014b; Yuk et al., 2016b). After degassing the precursor solution in a vacuum chamber, we added 8.2 µl N,N,N′,N′-tetramethylethylenediamine (Sigma, T7024-50M) into the total precursor solution of 10 ml as the crosslinking accelerator for acrylamide. We tuned the shear modulus μ of the sample as 1.1 kPa, 2.2 kPa, 3.0 kPa, 3.6 kPa, 11 kPa and 14 kPa by controlling both the concentration of polymer and crosslink density (see detailed material constituents in Fig. 2). By adopting the measured surface tension $\gamma = 0.07\,\mathrm{J/m^2}$ for PAAm hydrogel (Kundu and Crosby, 2009), we can set the elastocapillary length γ/μ for gel A, gel B , gel C, gel D, gel E and gel F as 65 μm, 32 μm, 23 μm, 19 μm, 6.5 μm and 5 μm respectively. To control the maximum defect size within the sample, we degassed the precursor solution first and mixed a controlled volume amount of nitrogen gas of 100 μl in one syringe with 10 ml total precursor solution in another syringe for 10 times. The maximum defect size within the sample can be well controlled as $A \sim 1\ \mu$m for the material with various constituents.

3.2. Mechanical testing

The experimental setup used in the current study is illustrated schematically in Fig. 1a. A layer of a soft yet stretchable hydrogel was robustly bonded onto two thick and transparent glass substrates (Yuk et al., 2016a). The diameter of the hydrogel layer D was varied from 6 mm to 140 mm and the thickness H from 1.5 mm to 6 mm, so that the aspect ratio of the elastic layer α was selected in a wide range from 1 to 50. During a typical test, the bottom glass substrate of the sample was fixed, and the top glass substrate was pulled upward at a controlled loading rate of 0.016 $\mathrm{s^{-1}}$ without causing any lateral displacement, using a universal material test machine (2 kN load cell for samples with diameter $D > 12$ mm and 20 N load cell for samples with diameter $D < 12$ mm; Zwick/Roell Z2.5). Both the applied force and the loading displacement was measured by the load cell and the deformation of the layer's free surfaces was recorded by cameras viewing from both side view and top view. To suppress the interfacial detachment, we used a functional silane, 3-(trimethoxysilyl) propyl methacrylate (TMSPMA), to modify the surfaces of transparent glass and then covalently crosslinked the long chain polymer network of polyacrylamide (PAAm) to the silanes on the modified surfaces of glass substrates (Yuk et al., 2016a). All the mechanical tests in this paper were performed in the air and measured in an “as-prepared” state.

3.3. Finite-element simulation

In addition to a set of systematic experimental studies, we performed corresponding numerical simulations to capture the deformation and instability of an elastic layer with the finite element method using ABAQUS/Explicit. To focus on a pure elastic behavior at relative short time scale, we modeled the hydrogel as a neo-Hookean material and suppressed the water diffusion in the hydrogel in the current study. We set the ratio between bulk modulus and shear modulus K/μ as large as we can, and in this case is 2000, to capture the incompressibility of the material. The type of element was taken as C3D8R and the mesh size was taken as small as $\sim 1/10$ of the smallest feature dimension for all samples to ensure the accuracy of the simulation. Additionally, a mass scaling technique was used to obtain results within a reasonable computation time. All numerical models have the same dimensions and loading setup as the experimental specimens.

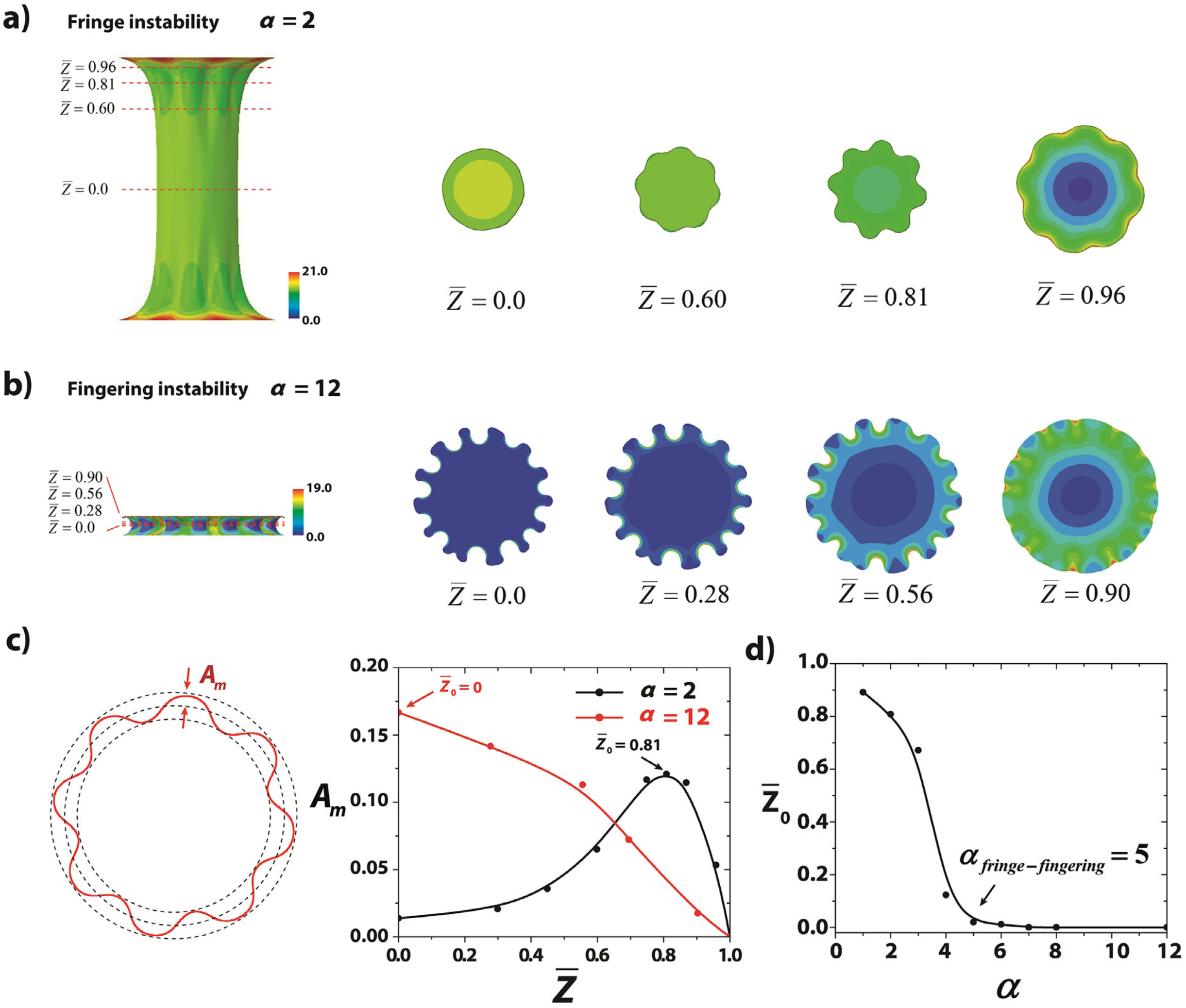

Fig. 3. Morphology difference between fringe instability and fingering instability. a) Undulation contours at the different planes right after the onset of fringe instability for the sample with $\alpha = 2$. Maximum amplitude occurs at $\bar{Z} = \pm 0.81$. b) Undulation contours at the different planes right after the onset of fingering instability for the sample with $\alpha = 12$. Maximum amplitude occurs at $\bar{Z} = 0$. c) The normalized amplitude of undulation contours versus $\bar{Z}$ right after the onset of instabilities for the sample with $\alpha = 2$ and $\alpha = 12$. d) The $\bar{Z}_0$ for the maximum amplitude of the undulation contours versus aspect ratios.

4. Modes of instabilities

Fig. 1c schematically illustrates the qualitative differences among fringe, fingering and cavitation instabilities. If the elastic layer's radius is comparable with or lower than its thickness (e.g., $\alpha < 4$), the free surfaces of the fringe portions of the layer gradually undulate into a periodic pattern under a critical applied stretch, giving the fringe instability (Lin et al., 2016). If the layer's aspect ratio is moderately high (e.g., $6 < \alpha < 20$), the deformed meniscus maintains a parabolic shape, until a spatially periodic pattern of air fingers invade the meniscus at a critical applied stretch (Biggins et al., 2013; Shull et al., 2000). If the layer's aspect ratio is extremely high (e.g., $\alpha > 30$) or the dimensionless elastocapillary number β is relatively low, a cavity nucleates and grows within the bulk sample prior to the formation of the undulating patterns on the exposed lateral surfaces.

While both fringe and fingering instabilities feature the undulation of the elastic layer's meniscus, they initiate at the fringe and middle portions of the meniscus, respectively. Therefore, the highest amplitude of the undulation for fringe and fingering, right after their initiation, is expected to appear at the fringe and middle portions of the meniscus, respectively (i.e. we take the vertical location that gives the highest undulation amplitude $\bar{Z}_0$ as the location where the undulations initiate in simulation). In Fig. 3a and b, we give the simulation results for fringe ($\alpha = 2$) and fingering ($\alpha = 12$) instabilities in elastic layers with different aspect ratios. We further quantify the undulation amplitude A_m for fringe ($\alpha = 2$) and fingering ($\alpha = 12$) instabilities as a function of the normalized vertical location $\bar{Z}$ (see Fig. 3c). Evidently, the highest amplitude of the undulation for fringe and fingering indeed appears at the fringe ($\bar{Z} = 0.81$) and middle ($\bar{Z} = 0$) portions of the meniscus, respectively. In Fig. 3d, we further plot the vertical location that gives the highest undulation amplitude $\bar{Z}_0$ as a function of the elastic layer's aspect ratio α, which shows that critical transition aspect ratio from fringe to fingering instability as $\alpha_{fringe-fingering} = 5$.

5. Theoretical analysis

In this part, we will develop a theory to understand i). the large deformation and stress fields in the constrained elastic layer under tension and ii). the critical points for the onset of fringe, fingering and cavitation instabilities. We first solve the equations of an incompressible neo-Hookean layer under tension and obtain the meniscus shapes, the applied stress–stretch relations, and the hydrostatic pressure versus stretch in the elastic layer. Thereafter, we perform the linear perturbation analysis to predict the critical stretch λ_c and the critical stress S_c for the onset of both fringe instability and fingering instability.

5.1. Large deformation and stress fields in constrained elastic layers under tension

Geometrically, the elastic layer in the un-deformed state occupies a region $0 \le R \le D/2$, $0 \le \Theta < 2\pi$ and $-H/2 \le Z \le H/2$. A material particle in the layer is labeled by its coordinate (R, Θ, Z) in the un-deformed state with $\{\mathbf{e}_R, \mathbf{e}_\Theta, \mathbf{e}_Z\}$ as the basis in cylindrical coordinate (see Fig. 1b). In the deformed state, the material particle moves to a place of coordinates (r, θ, z), which are functions of (R, Θ, Z). Since the elastic layer deforms axisymmetrically prior to instability, the displacement in Θ direction $u_\Theta = 0$ and the displacement in radius direction u_R and that in axial direction u_Z are independent of Θ. Here, we make a single assumption on the deformation of the layer, that is: *any horizontal plane in the layer at the un-deformed state remains planar upon deformation* (Klingbeil and Shield, 1966; Lin et al., 2016; Shariff, 1989). Based on the axisymmetric deformation, horizontal-plane assumption and incompressibility of the material, we can specify the displacement field in the elastic layer as

$$u_R(\bar{R}, \bar{Z}) = \bar{R}u_1(\bar{Z}), \tag{3}$$

$$u_Z(\bar{Z}) = u_2(\bar{Z}), \tag{4}$$

with $\bar{R} = \frac{R}{D/2}$, $\bar{Z} = \frac{Z}{H/2}$. The linear dependence of u_R on $\bar{R}$ is directly from the horizontal plane assumption with the incompressibility. Using the displacement field in Eq. (3) and Eq. (4), we can express the deformation gradient in the layer as:

$$\mathbf{F} = \begin{bmatrix} \lambda_{rR} & 0 & \gamma_{rZ} \\ 0 & \lambda_{\theta\Theta} & 0 \\ 0 & 0 & \lambda_{zZ} \end{bmatrix}, \tag{5a}$$

with

$$\lambda_{rR} = 1 + \frac{1}{D/2}u_1, \tag{5b}$$

$$\lambda_{\theta\Theta} = 1 + \frac{1}{D/2}u_1, \tag{5c}$$

$$\lambda_{zZ} = 1 + \frac{1}{H/2}u_2', \tag{5d}$$

$$\gamma_{rZ} = \frac{1}{H/2}\bar{R}u_1', \tag{5e}$$

with the prime for differentiating respect to $\bar{Z}$, or explicitly, $u_1' = \frac{du_1}{d\bar{Z}}$ and $u_2' = \frac{du_2}{d\bar{Z}}$. The incompressibility of the elastic layer also enforces the conservation of volume, which reads as:

$$\det(\mathbf{F}) = \lambda_{rR}\lambda_{\theta\Theta}\lambda_{zZ} = 1. \tag{6}$$

The elastic layer is taken as an incompressible neo-Hookean solid with strain energy density function $\psi = \frac{\mu}{2}[\mathrm{tr}(\mathbf{F}^{\mathrm{T}}\mathbf{F}) - 3]$. Therefore, the nominal stress tensor $\mathbf{S}$ is expressed through $\mathbf{S} = \mu\mathbf{F} - p^*\mathbf{F}^{-\mathrm{T}}$ and the Cauchy stress tensor is expressed through $\boldsymbol{\sigma} = \mathbf{S}\mathbf{F}^{\mathrm{T}}$, namely:

$$\mathbf{S}/\mu = \begin{pmatrix} \lambda_{rR} - \bar{p}/\lambda_{rR} & 0 & \gamma_{rZ} \\ 0 & \lambda_{\theta\Theta} - \bar{p}/\lambda_{\theta\Theta} & 0 \\ \lambda_{\theta\Theta}\gamma_{rZ}\bar{p} & 0 & \lambda_{zZ} - \bar{p}/\lambda_{zZ} \end{pmatrix}, \tag{7a}$$

$$\boldsymbol{\sigma}/\mu = \begin{pmatrix} \lambda_{rR}^2 - \bar{p} + \gamma_{rZ}^2 & 0 & \gamma_{rZ}\lambda_{zZ} \\ 0 & \lambda_{\theta\Theta}^2 - \bar{p} & 0 \\ \gamma_{rZ}\lambda_{zZ} & 0 & \lambda_{zZ}^2 - \bar{p} \end{pmatrix}, \tag{7b}$$

where p^* is the Lagrange multiplier to enforce the incompressibility and $\bar{p} = p^*/\mu$ is the corresponding dimensionless form. The equilibrium equations read Div $\mathbf{S}$=$\mathbf{0}$. Since the equilibrium equation along the hoop direction will be satisfied automatically, then the remaining equilibrium equations along radius direction and axial direction are

$$-\frac{1}{\lambda_{rR}}\frac{\partial \bar{p}}{\partial \bar{R}} + \alpha\frac{\partial \gamma_{rZ}}{\partial \bar{Z}} = 0, \tag{8}$$

$$\lambda_{rR}\frac{\partial(\gamma_{rZ}\bar{p})}{\partial \bar{R}} + \frac{\lambda_{rR}\gamma_{rZ}\bar{p}}{\bar{R}} + \alpha\frac{\partial(\lambda_{zZ} - \bar{p}/\lambda_{zZ})}{\partial \bar{Z}} = 0, \tag{9}$$

with $\alpha = D/H$. Since the highest order of $\bar{R}$ in γ_{rZ} is linear and in order to satisfy Eq. (8), $\bar{p}$ should be a function of $\bar{R}^2$. With this observation, we can solve both Eq. (8) and Eq. (9) analytically (see Appendix A.1 for more details). By imposing the boundary conditions: $\mathrm{d}u_1/\mathrm{d}\bar{Z}|_{\bar{Z}=0} = 0$, $u_1(\bar{Z} = \pm 1) = 0$ and $u_2(\bar{Z} = 0) = 0$, the specific functions $u_1(\bar{Z})$ and $u_2(\bar{Z})$ can be identified as

$$u_1(\bar{Z}) = \frac{D}{2}\left[\frac{\cosh(\kappa\bar{Z})}{\cosh(\kappa)} - 1\right], \tag{10a}$$

$$u_2(\bar{Z}) = \frac{H}{2}\left[\frac{\sinh(2\kappa)}{2\kappa}\frac{\tanh(\kappa\bar{Z})}{\tanh(\kappa)} - \bar{Z}\right], \tag{10b}$$

where κ is an internal loading parameter which is correlated with the applied stretch through

$$\lambda = \frac{\sinh(2\kappa)}{2\kappa}. \tag{10c}$$

With the calculated functions of $u_1(\bar{Z})$ and $u_2(\bar{Z})$, we further plot the meniscus shape at various stretches for the sample with $\alpha = 4$ and $\alpha = 8$ shown in Fig. 4. Our analytical results match well with the numerical results from 2D asymmetrical finite-element model. At small stretches (e.g. $\lambda = 1.5$ for $\alpha = 4$), the meniscus shape is parabolic (Biggins et al., 2013); while as stretch becomes large (e.g. $\lambda = 2.5$ for $\alpha = 4$), the meniscus shape deviates from the parabolic profile severely and the middle portion of the sample is almost uniformly deformed as discussed in previous report (Lin et al., 2016).

With the specified functions of $u_1(\bar{Z})$ and $u_2(\bar{Z})$, we can further calculate the dimensionless Lagrange multiplier $\bar{p}$ in the form of (see details in Appendix. A.1):

$$\bar{p}\left(\bar{R}, \bar{Z}\right) = q_0\left(\bar{Z}\right) + \left(\bar{R}^2 - 1\right)q_1\left(\bar{Z}\right), \tag{11a}$$

with

$$q_0\left(\bar{Z}\right) = \frac{\cosh^2(\kappa\bar{Z})}{2\cosh^2\kappa}\kappa^2\alpha^2 + \frac{\cosh^4\kappa}{2\cosh^4(\kappa\bar{Z})} + C_3, \tag{11b}$$

$$q_1\left(\bar{Z}\right) = \frac{\cosh^2(\kappa\bar{Z})}{2\cosh^2\kappa}\kappa^2\alpha^2, \tag{11c}$$

where C_3 is to be determined by a boundary condition.

Owning to the assumption that any horizontal plane in the layer at the un-deformed state remains planar upon deformation, it's impossible to satisfy the traction free boundary conditions for the whole exposed surfaces (i.e. at any height of the sample). Here, since we specifically focus on the case when the instabilities initiates at exact the middle plane or closer to the middle plane, we enforce the boundary condition at $\bar{Z} = 0$, namely the traction $\mathbf{t}_R = \mathbf{S} \cdot \mathbf{e}_R$ shall be zero at $\bar{R} = 1$ and $\bar{Z} = 0$, where $\{\mathbf{e}_R, \mathbf{e}_\Theta, \mathbf{e}_Z\}$ is the basis in cylindrical coordinate. Since $S_{\theta R} = S_{zR} = 0$ owing to the symmetric condition at the middle plane, the only boundary condition needs to be satisfied is $S_{rR} = \mu(\lambda_{rR} - \bar{p}/\lambda_{rR}) = 0$ at the middle plane. Therefore, constant C_3 can be identified as:

$$C_3 = \frac{1}{\cosh^2\kappa}\left(1 - \frac{1}{2}\kappa^2\alpha^2\right) - \frac{1}{2}\cosh^4\kappa, \tag{12}$$

and full expression of dimensionless Lagrange multiplier reads as

$$\bar{p} = \frac{1}{2}\left(\frac{\cosh^4\kappa}{\cosh^4\left(\kappa\bar{Z}\right)} - \cosh^4\kappa\right) + \frac{\kappa^2\alpha^2}{2}\left(\bar{R}^2\frac{\cosh^2\left(\kappa\bar{Z}\right)}{\cosh^2\kappa} - \frac{1}{\cosh^2\kappa}\right) + \frac{1}{\cosh^2\kappa}. \tag{13}$$

We further calculate the averaged nominal stress applied on the layer S through

$$S = \frac{4}{H\pi D^2} \cdot \frac{dW}{d\lambda}, \tag{14}$$

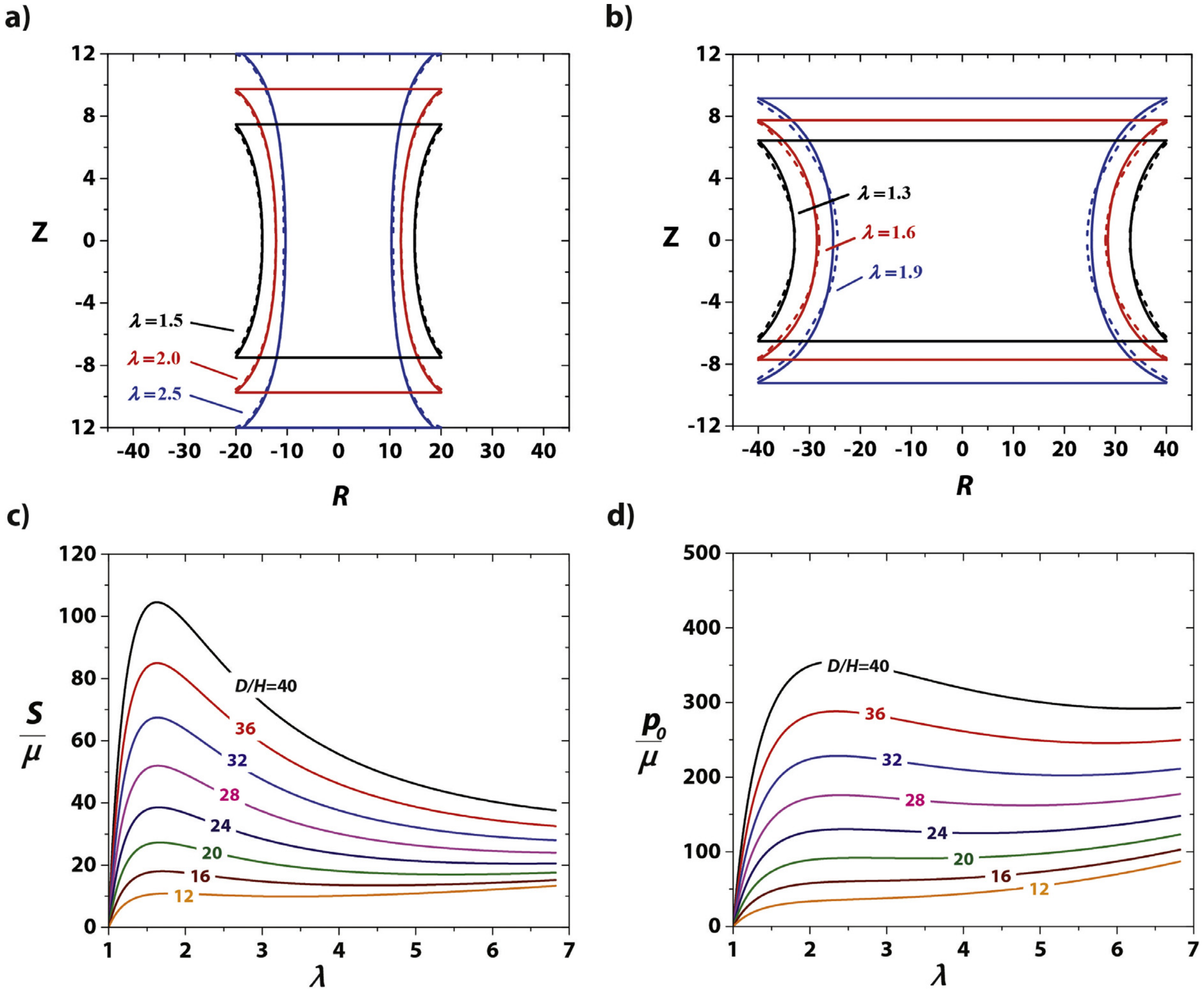

Fig. 4. Theoretical and simulation results on the deformation and stress fields in constrained neo-Hookean layers under tension. a) Comparison between theory and simulation of the meniscus profiles for the sample with aspect ratio of $\alpha = 4$ at the stretch of $\lambda = 1.5$, $\lambda = 2.0$ and $\lambda = 2.5$. Solid line represents the theoretical results; dashed line represents the simulation results. b) Comparison between theory and simulation of the meniscus profiles for the sample with aspect ratio of $\alpha = 8$ at the stretch of $\lambda = 1.3$, $\lambda = 1.6$ and $\lambda = 1.9$. Solid line represents the theoretical results; dashed line represents the simulation results. c) Theoretically calculated applied nominal stress versus stretch for the samples with various aspect ratios. d) Theoretically calculated hydrostatic pressure at the center of the samples versus stretch for the sample with various aspect ratios.

where W is the total elastic energy of the layer which can be calculated by integrating ψ over the volume of the layer: $W = 2\int_0^{\frac{H}{2}}\int_0^{\frac{D}{2}} 2\pi R\psi(R,Z)dRdZ$. After algebraic simplification, the applied nominal stress S can be expressed as:

$$S/\mu = S_0(\kappa) + \alpha^2 S_1(\kappa), \tag{15}$$

where both S_0 and S_1 are functions of a single variable with respect to the loading parameter κ (see detailed expressions in Appendix A.1). As shown in Fig. A.1, S_0 monotonically increases with the applied stretch, while S_1 is non-monotonic with a peak point at $\kappa = 0.89$ (i.e. $\lambda = 1.62$). When α is very small, S_0 is dominated, and there is no peak displayed in the stress–stretch curve. With the increase of aspect ratio α, the second term $\alpha^2 S_1$ will gradually become dominated and a peak stress will display in the overall applied stress–stretch curve which is associated with the global necking mode (Lin et al., 2016). The overall S/μ curves for various α are shown in Fig. 4c. In Fig. A.2a, we further show that the initial slope of our curves agrees with the result from the calculations based on small deformation (Gent and Lindley, 1959a; Klingbeil and Shield, 1966; Tupholme and Gover, 2002) .

Next, we derive the hydrostatic pressure at the center of the sample, which is given by $p_0 = p(\bar{Z} = 0, \bar{R} = 0) = \frac{1}{3}\mathrm{tr}(\boldsymbol{\sigma})|_{\bar{Z}=0,\bar{R}=0}$ where $\boldsymbol{\sigma} = \mathbf{SF}^{\mathrm{T}}$ is the Cauchy stress tensor. From Eq. (7b), the expression of the hydrostatic pressure can be expressed as:

$$p_0/\mu = \frac{\lambda_{rR}^2 + \lambda_{\theta\Theta}^2 + \lambda_{zZ}^2 + \gamma_{rZ}^2}{3} - \bar{p}. \tag{16}$$

Inserting $\lambda_{rR}(\bar{Z}=0)=\lambda_{\theta\Theta}(\bar{Z}=0)=\frac{1}{\cosh\kappa}$, $\lambda_{zZ}(\bar{Z}=0)=\cosh^2\kappa$, $\gamma_{rZ}(\bar{R}=0,\bar{Z}=0)=0$ and $\bar{p}(\bar{R}=0,\bar{Z}=0)=\frac{1}{\cosh^2\kappa}-\frac{\kappa^2\alpha^2}{2\cosh^2\kappa}$, one can write the hydrostatic pressure at the center of the sample as

$$p_0/\mu=\frac{\cosh^4(\kappa)}{3}-\frac{1}{3\cosh^2(\kappa)}+\frac{\kappa^2\alpha^2}{2\cosh^2(\kappa)} \tag{17}$$

The p_0/μ vs. λ curves for elastic layers with various aspect ratios α are shown in Fig. 4d. To validate our results, we calculate $\frac{1}{\mu}\frac{dp_0}{d\lambda}|_{\lambda=1}$ and compare it with the reported small-strain solutions (Klingbeil and Shield, 1966), which shows good agreement (see Fig. A.2b).

As a summary of this part, we have developed an analytical model to account for the large deformation of a constrained incompressible neo-Hookean layer under tension. The model gives analytic results on the deformation (Eq. (10), Fig. 4a and b), the applied nominal stress (Eq. (15), Fig. 4c), and the hydrostatic pressure at the center of the layer (Eq. (17), Fig. 4d) as functions of the applied stretch on the layer. Our analytical model is validated by the results from numerical simulations and reported small-deformation solutions.

5.2. Onset of fringe and fingering instabilities

In this section, we will use the perturbation analysis to calculate the critical points for the onset of fringe and fingering instabilities. We introduce a trial form for the solutions consisting of the rotational invariant part at base state solved in Section 5.1 and an infinitesimal oscillatory part. The fields of deformation and Lagrange multiplier with first order perturbation read as:

$$\mathbf{x}=(\mathbf{x})^0+\varepsilon\tilde{\mathbf{x}}, \tag{18}$$

$$\bar{p}=(\bar{p})^0+\varepsilon\tilde{p}, \tag{19}$$

where ε is a dimensionless small parameter, $\tilde{\mathbf{x}}$ and $\tilde{p}$ are perturbed fields, $(\mathbf{x})^0$ and $(\bar{p})^0$ are the rotational invariant fields at base state, which is solved in Section 5.1 in the cylindrical basis $\{\mathbf{e}_R,\mathbf{e}_\Theta,\mathbf{e}_Z\}$ as:

$$(\mathbf{x})^0=\frac{D\bar{R}}{2}\left[\frac{\cosh(\kappa\bar{Z})}{\cosh(\kappa)}-1\right]\mathbf{e}_R+\frac{H}{2}\left[\frac{\sinh(2\kappa)}{2\kappa}\frac{\tanh(\kappa\bar{Z})}{\tanh(\kappa)}-\bar{Z}\right]\mathbf{e}_Z, \tag{20}$$

$$(\bar{p})^0=\frac{1}{2}\left[\frac{\cosh^4\kappa}{\cosh^4\left(\kappa\bar{Z}\right)}-\cosh^4\kappa\right]+\frac{\kappa^2\alpha^2}{2}\left[\bar{R}^2\frac{\cosh^2\left(\kappa\bar{Z}\right)}{\cosh^2\kappa}-\frac{1}{\cosh^2\kappa}\right]+\frac{1}{\cosh^2\kappa}. \tag{21}$$

We assume the perturbed displacement field and the perturbed Lagrange multiplier follow the forms,

$$\tilde{\mathbf{x}}=A_1(R)u_1(Z)\cos(\omega\Theta)\mathbf{e}_R+A_2(R)u_1(Z)\sin(\omega\Theta)\mathbf{e}_\Theta+A_3(R)u_2(Z)\sin(\omega\Theta)\mathbf{e}_Z, \tag{22}$$

$$\tilde{p}=A_4(Z,R)\cos(\omega\Theta), \tag{23}$$

where A_i ($i=1,2,3,4$) are the amplitudes of perturbation. Therefore, the perturbed deformation gradient may write as $\mathbf{F}=(\mathbf{F})^0+\varepsilon\mathrm{Grad}\tilde{\mathbf{x}}$, where $(\mathbf{F})^0$ is the rotational invariant deformation gradient at base state expressed in Eq. (5). By inserting the perturbed displacement field, the deformation gradient reads as:

$$\mathbf{F}=\begin{bmatrix}\lambda_{rR}+\varepsilon A_1'u_1\cos(\omega\Theta) & -\varepsilon\frac{A_1\omega+A_2}{R}u_1\sin(\omega\Theta) & \gamma_{rZ}+\varepsilon A_1u_1'\cos(\omega\Theta)\\ \varepsilon A_2'u_1\sin(\omega\Theta) & \lambda_{\theta\Theta}+\varepsilon\frac{A_2\omega+A_1}{R}u_1\cos(\omega\Theta) & \varepsilon A_2u_1'\sin(\omega\Theta)\\ \varepsilon A_3'u_2\cos(\omega\Theta) & -\varepsilon\frac{A_3\omega}{R}u_2\sin(\omega\Theta) & \lambda_{zZ}+\varepsilon A_3u_2'\cos(\omega\Theta)\end{bmatrix}. \tag{24}$$

Here the prime represents for differentiating respects to R or Z, i.e. $A_1'=\frac{dA_1}{dR}$, $A_2'=\frac{dA_2}{dR}$, $A_3'=\frac{dA_3}{dR}$, $u_1'=\frac{du_1}{dZ}$ and $u_2'=\frac{du_2}{dZ}$. The incompressibility of the elastic layer is enforced by $\det\mathbf{F}=1$, which implies (expand to the first order of ε, see details in Appendix A.2):

$$\lambda_{zZ}A_1'u_1+\lambda_{zZ}\frac{A_2\omega+A_1}{R}u_1-\gamma_{rZ}A_3'u_2+\lambda_{rR}A_3u_2'=0. \tag{25}$$

The perturbation in deformation gradient will further induce a perturbation in nominal stress which reads as $\mathbf{S}/\mu=(\mathbf{S})^0/\mu+\varepsilon\tilde{\mathbf{S}}$. Here, $\tilde{\mathbf{S}}$ is the perturbed normalized nominal stress, and each component of which is expressed as:

$$\tilde{S}_{rR}=\left[A_1'u_1-(\bar{p})^0\left(\gamma_{rZ}A_3'u_2-\lambda_{zZ}A_1'u_1\right)-\frac{A_4}{\lambda_{rR}}\right]\cos(\omega\Theta), \tag{26a}$$

$$\tilde{S}_{r\Theta} = \left[-\frac{A_1\omega + A_2}{R} u_1 + (\bar{p})^0 \lambda_{zZ} A_2' u_1 \right] \sin(\omega\Theta), \tag{26b}$$

$$\tilde{S}_{rZ} = \left[A_1 u_1' + (\bar{p})^0 \lambda_{rR} A_3' u_2 \right] \cos(\omega\Theta), \tag{26c}$$

$$\tilde{S}_{\theta R} = \left[A_2' u_1 - (\bar{p})^0 \lambda_{zZ} \frac{A_1\omega + A_2}{R} u_1 + (\bar{p})^0 \gamma_{rZ} \frac{A_3\omega}{R} u_2 \right] \sin(\omega\Theta), \tag{26d}$$

$$\tilde{S}_{\theta\Theta} = \left[\lambda_{rR}^2 \gamma_{rZ} A_3' u_2 - \lambda_{rR}^3 A_3 u_2' - A_1' u_1 - (\bar{p})^0 \left(\lambda_{zZ} A_1' u_1 - \gamma_{rZ} A_3' u_2 + \lambda_{rR} A_3 u_2' \right) - \frac{A_4}{\lambda_{rR}} \right] \cos(\omega\Theta), \tag{26e}$$

$$\tilde{S}_{\theta Z} = \left[A_2 u_1' - (\bar{p})^0 \lambda_{rR} \frac{A_3\omega}{R} u_2 \right] \sin(\omega\Theta), \tag{26f}$$

$$\tilde{S}_{zR} = \left[A_3' u_2 + \lambda_{rR} \gamma_{rZ} A_4 + (\bar{p})^0 \gamma_{rZ} \left(\lambda_{rR}^2 \gamma_{rZ} A_3' u_2 - \lambda_{rR}^3 A_3 u_2' - A_1' u_1 \right) + (\bar{p})^0 \lambda_{rR} A_1 u_1' \right] \cos(\omega\Theta), \tag{26g}$$

$$\tilde{S}_{z\Theta} = \left[-\frac{A_3\omega}{R} u_2 - (\bar{p})^0 \gamma_{rZ} A_2' u_1 + (\bar{p})^0 \lambda_{rR} A_2 u_1' \right] \sin(\omega\Theta), \tag{26h}$$

$$\tilde{S}_{zZ} = \left[A_3 u_2' - \lambda_{rR}^2 A_4 - (\bar{p})^0 \lambda_{rR} u_1 \left(A_1' + \frac{A_2\omega + A_1}{R} \right) \right] \cos(\omega\Theta), \tag{26i}$$

A balance of the forces exerted on an element of the perturbed material further leads to three equations of equilibrium Div $\tilde{\mathbf{S}} = 0$. These equations are only required to satisfy in $\bar{Z} = \bar{Z}_0$ with $\bar{Z}_0$ being the vertical location where the undulations initiates. The four unknown A_i $(i = 1, 2, 3, 4)$ can be fully specified by these three equations and the incompressibility condition in Eq. (25) with boundary conditions. The boundary conditions are still the traction $\mathbf{t}_R = \mathbf{S} \cdot \mathbf{e}_R$ be zero at $\bar{R} = 1$ (For cases when $\bar{Z}_0 \neq 0$, this is an approximation). Since the rotational invariant stress at base state already satisfies the boundary conditions, then we have $\tilde{\mathbf{S}} \cdot \mathbf{e}_R = 0$ at $\bar{R} = 1$. Also we are looking for the solution which decays as $\bar{R} \to 0$ (see details in Appendix A.2).

By simplifying the four equations through eliminating A_2 and A_4, we can finally obtain two governing equations in the dimensionless form with respect to A_1 and A_3 (for more details, see Appendix A.2). We can solve these equations by numerically or even analytically with infinite series. However, to obtain the physical insight, we choose to make some approximations to simplify the equations. We notice the difference between fingering and fringe instabilities: fingering instability is an instability mode with $A_3 = 0$ (see Fig. A.3a) while the fringe instability is an instability mode with generally $A_3 \neq 0$ (see Fig. A.3b). Physically, the zero amplitude along Z direction for fingering instability is a consequence of symmetry. For fringe instability, we argue that if α is slightly smaller than the theoretical transition aspect ratio $\alpha_{fringe-fingering}$ between fingering instability and fringe instability, $A_3 \ll A_1$ and $A_3 \ll A_2$, or explicitly $A_3 \approx 0$. By adopting this approximation, the only governing ODE to be solved is with respect to the amplitude along radius direction A_1 in the dimensionless form, reading as (see details in Appendix A.2. For dimensionless form, the prime is for differentiating respect to $\bar{R}$):

$$\begin{aligned} &\bar{R}^4 A_1^{(4)} + 6\bar{R}^3 A_1^{(3)} + \left(5 - 2\omega^2\right) \bar{R}^2 A_1'' - \left(2\omega^2 + 1\right) \bar{R} A_1' + \left(\omega^2 - 1\right)^2 A_1 \\ &-A_h^2 \bar{R}^2 \left[\bar{R}^2 A_1'' + 3\bar{R} A_1' - \left(\omega^2 - 1\right) A_1 \right] = 0, \end{aligned} \tag{27}$$

with $A_h = \sqrt{\frac{\kappa^2\alpha^2}{1-\lambda_{rR}}}$. Next we impose the boundary conditions on this governing ODE. The boundary condition of $\tilde{S}_{zR} = 0$ automatically satisfies with the condition that $A_3 \ll A_1$ and $A_3 \ll A_2$. The remaining two boundary conditions in the dimensionless form read as:

$$A_1^{(3)}(1) + 4A_1''(1) + \left[1 - 2\omega^2 - \zeta\omega^2 - A_h^2\right] A_1'(1) + \left[\omega^2 - 1 + \omega^2\kappa^2\alpha^2 - A_h^2\right] A_1(1) = 0, \tag{28a}$$

$$A_1''(1) + (2 - \zeta) A_1'(1) + \zeta\left(\omega^2 - 1\right) A_1(1) = 0, \tag{28b}$$

with

$$\zeta(\bar{Z}_0) = \frac{1}{2}\kappa^2\alpha^2 + \frac{1}{2}\lambda_{rR}^{-6} + C_3\lambda_{rR}^{-2}, \tag{28c}$$

$$C_3 = \frac{1}{\cos^2\kappa}\left[1 - \frac{1}{2}\kappa^2\alpha^2\right] - \frac{1}{2}\cos^4\kappa. \tag{28d}$$

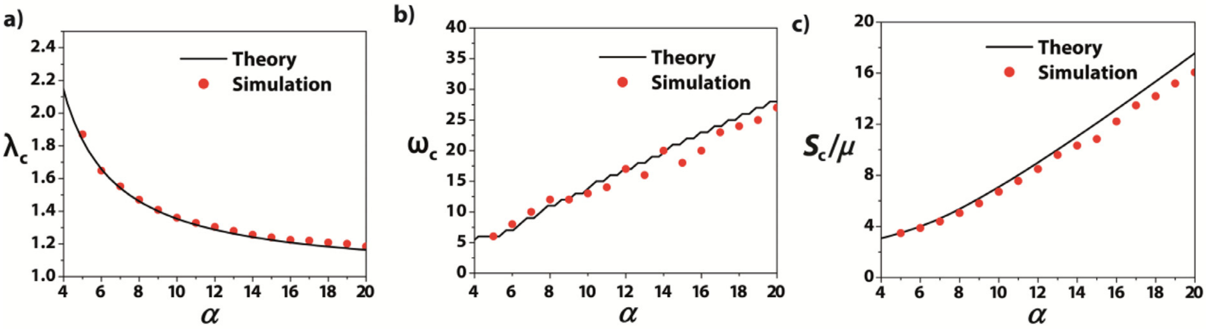

Fig. 5. Theoretical and simulation results on the critical points of fingering instability and fringe instability for the sample with aspect ratios $\alpha > 4$. a) Comparison of the critical stretch λ_c for the onset of instabilities between theory and simulation. b) Comparison of the critical mode number ω_c between theory and simulation. a) Comparison of the critical applied stress S_c between theory and simulation.

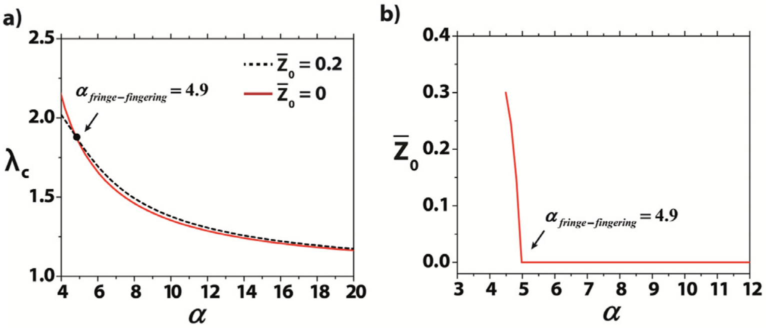

Fig. 6. Theoretical results on the transition between fringe and fingering instability. a) Critical stretch for the sample with the locations for the initiation of undulations at $\bar{Z}_0 = 0$ and $\bar{Z}_0 = 0.2$. b) The location of the initiation of the instabilities $\bar{Z}_0$ for the sample with different aspect ratios.

There are four characteristic roots for Eq. (27): two of them are decay solutions (decreases as $\bar{R} \to 0$) and the other two are non-decay (diverges as $\bar{R} \to 0$). The two non-decay solutions vanish. After going through the algebra, the general solution of A_1 can be written as (see details in Appendix A.2):

$$A_1 = c_1\bar{R}^{\omega-1} + c_2\frac{1}{I_\omega(A_h)}I_\omega\left(A_h\bar{R}\right)\bar{R}^{-1}, \tag{29}$$

where $I_\omega(\bullet)$ is the modified Bessel function of the first kind, c_1 and c_2 are arbitrary pre-factors (see details in Appendix A.2). Insert this solution into the two boundary conditions in Eq. (28a) and Eq. (28b), The existence of the non-trivial solution depends on whether the following equation has solution or not:

$$\begin{aligned}&\left(l^2\omega^3A_h + lA_h^3 - l^2\omega A_h\right)\frac{I_{\omega-1}(A_h)}{I_\omega(A_h)} - \left(2l\omega^2A_h^2 + 2l^2\omega^4 - 2l^2\omega^2 + A_h^4\right)\\&+\left(2l\omega^2 + \omega A_h^2 - l\omega A_h\frac{I_{\omega-1}(A_h)}{I_\omega(A_h)}\right)\kappa^2\alpha^2 = 0,\end{aligned} \tag{30}$$

where $l = 1 + \zeta$.

By minimizing κ through ω at each plane $\bar{Z}$, we can have the critical stretch λ_c, the critical number of undulations ω_c and the vertical location of the plane where the undulations initiate $\bar{Z}_0$. As shown in Fig. 5a and b, our theory predicts quite well for both λ_c and ω_c at the onset of instabilities in the range $\alpha > 4$, comparing with the simulation results. With the deformation field we derived in Section 5.1, we further predict the critical applied nominal stress S_c for the onset of instabilities shown in Fig. 5c. Our theory with incompressible assumption is slightly higher than the simulation results with negligible compressibility (in simulation, bulk modulus is set 2000 times the shear modulus, i.e. $K/\mu = 2000$), which is reasonable.

Moreover, to theoretically identify the critical geometrical aspect ratio between fringe instability and fingering instability $\alpha_{fringe-fingering}$, we compare the critical stretch for the case with initial location of undulations at $\bar{Z}_0 = 0$ and $\bar{Z}_0 \neq 0$. If the critical stretch for the case $\bar{Z}_0 = 0$ is the smallest, then fingering instability will be triggered first. On the other hand, if the critical stretch for the case $\bar{Z}_0 = 0$ is not the smallest, fringe instability will be triggered first and fingering instability will be suppressed. Fig. 6a presents the critical stretch for both cases with $\bar{Z}_0 = 0$ and $\bar{Z}_0 = 0.2$ calculated from Eq. (30) as an example. As show in Fig. 6a, when α is below a critical value, fringe instability will be more favorable than fingering instability. In order to identify the boundary between these two instabilities, we plot the location of the initiation of the instabilities for layers with various aspect ratios α. In the current work, we focus on the case with very small $\bar{Z}_0$ (i.e. $\bar{Z}_0 \leq 0.3$). As we can see in Fig. 6b, when $\alpha > 4.9$, the initiation of the instability occurs at the middle plane, which is the case of fingering instability. In contrast, when $\alpha < 4.9$, the lower critical stretch is identified at $\bar{Z}_0 \neq 0$, which is corresponding to fringe instability. Therefore, the theoretically calculated critical transition between fingering instability and fringe instability is identified as 4.9, which agrees with the simulation results (i.e. $\alpha_{fringe-fingering} = 5$) discussed in Section 4.

5.3. Onset of cavitation instability

Cavitation is the another mode of mechanical instability emerging in elastic layers under tension, as the hydrostatic pressure in the layer reaches a critical value (Ball, 1982; Gent, 1990). Theoretical explanation of the nucleation and growth of a cavity within a bulk material has been intensively studied, which was either considered as a process of creation of a new surface representing fracture (Long and Hui, 2010) or regarded as an elastic instability of a pre-existing cavity undergoing hydrostatic pressure (Biwa, 2006; Dollhofer et al., 2004; Lefèvre et al., 2015). Here, we take the emergence of cavity as an elastic instability and adopt the bifurcation theory (Biwa, 2006) to calculate the critical hydrostatic traction on the pre-existing cavity for the onset of cavitation instability in an incompressible Neo-Hookean solid (Dollhofer et al., 2004).

For a cavity under uniform hydrostatic traction T, by analyzing the force balance on the spherical shell surrounding the cavity with outer surface of $B \gg A$ (see Fig. 7a), the relation between the applied hydrostatic traction T and the expansion of the cavity can be expressed as (Dollhofer et al., 2004):

$$\frac{T}{\mu} = \frac{2\beta}{\lambda_A} - \frac{2}{\lambda_A} - \frac{1}{2\lambda_A^4} + \frac{2}{\lambda_R} + \frac{1}{2\lambda_R^4}, \tag{31}$$

where $\lambda_A = \frac{a}{A}$, $\beta = \frac{\gamma}{\mu A}$ and $\lambda_R = (1 - f^3 + f^3\lambda_A^3)^{1/3}$ with $f = \frac{B}{A}$ comes from the constraints of volume conservation. In this study, f is set as 1000, which is sufficient large to ensure that the result is independent of B (as $B \gg A$). From this expression, we can see that the expansion of a cavity highly depends on the dimensionless elastocapillary number β (Ball, 1982; Zimberlin and Crosby, 2010; Zimberlin et al., 2007). For example, if $\beta < 1$, the critical hydrostatic traction T_c approaches to 2.5μ and the cavity grows gradually with the increase of the hydrostatic traction T, which is the common case for rubbers. However, if $\beta \gg 1$, the applied hydrostatic traction T first increases dramatically with a negligible expansion of the cavity up to a maximum critical value shown in Fig. 7b, and thereafter the cavity bifurcates to a stable state suddenly with a large expansion ratio (Biwa, 2006; Dollhofer et al., 2004). The maximum hydrostatic traction T_c determines the critical point for the onset of cavitation instability. As shown in Fig. 7c, the effect of surface tension can enhance the critical hydrostatic traction T_c by multiple times, which is common for soft hydrogels with relative high dimensionless capillary number β (Zimberlin et al., 2007).

When a cylindrical layer is under tension as illustrated in Fig. 7a, the pre-existing cavity within the layer can be approximated in the state of uniform hydrostatic stress if the layer's aspect ratio is relative large (e.g. $\alpha > 5$) (Hang-Sheng and Abeyaratne, 1992; Stringfellow and Abeyaratne, 1989). Specifically focusing on the center of the layer with the highest chance of emergence of cavitation, when the hydrostatic pressure p_0 reaches the critical hydrostatic traction T_c shown in Fig. 7c, cavitation instability sets in the layer. To identify the critical applied stress S_c or the applied stretch λ_c for the onset of cavitation, we recall Eq. (15) and Eq. (17) derived in Section 5.1 and calculate the correlation between the applied nominal stress S or the applied nominal stretch λ and the hydrostatic pressure at the center of the sample p_0 for various aspect ratios α in Fig. 7d and e. In the limiting case of $\alpha \to \infty$, our theory is reduced to $S = \frac{p_0}{2}$, which is consistent with the reported results (Fond, 2001). We summarize the calculated critical stress S_c and the critical stretch λ_c for the layers with various aspect ratio α and dimensionless capillary number β shown in Fig. 7f and g. The critical nominal stress S_c for the onset of cavitation instability weakly dependent on layers' aspect ratio α while the critical stretch λ_c decreases dramatically as the increase of layers' aspect ratio α. For a layer with relatively small aspect ratios (e.g. $\alpha < 5$), there will be no cavitation emerging owning to the non-symmetric stress state (Gent and Lindley, 1959b; Hang-Sheng and Abeyaratne, 1992) and therefore only fringe instability sets in with the increase of the applied load.

To further theoretically calculate the critical transition aspect ratio from fingering to cavitation $\alpha_{fingering-cavitation}$, we plot the critical applied stress for both fingering instability and cavitation instability with various dimensionless capillary number β (see Fig. 8a). The intersections of both curves identify the critical transition aspect ratio from fingering to cavitation $\alpha_{fingering-cavitation}$for the samples with various β. As shown in Fig. 8b, the correlation between $\alpha_{fingering-cavitation}$ and β can be fitted simply by a linear relation:

$$\alpha_{fingering-cavitation} = 1.7\beta - 2.5, \quad \alpha > 5. \tag{32}$$

6. Evolution of instabilities

In Section 5, we use linear perturbation analysis to calculate the critical points for the onset of fringe instability and fingering instability. In this section, we further use simulation and experiment to discuss the evolution of fringe and fingering instabilities after their onsets and their corresponding applied stress–stretch relations (S vs. λ).

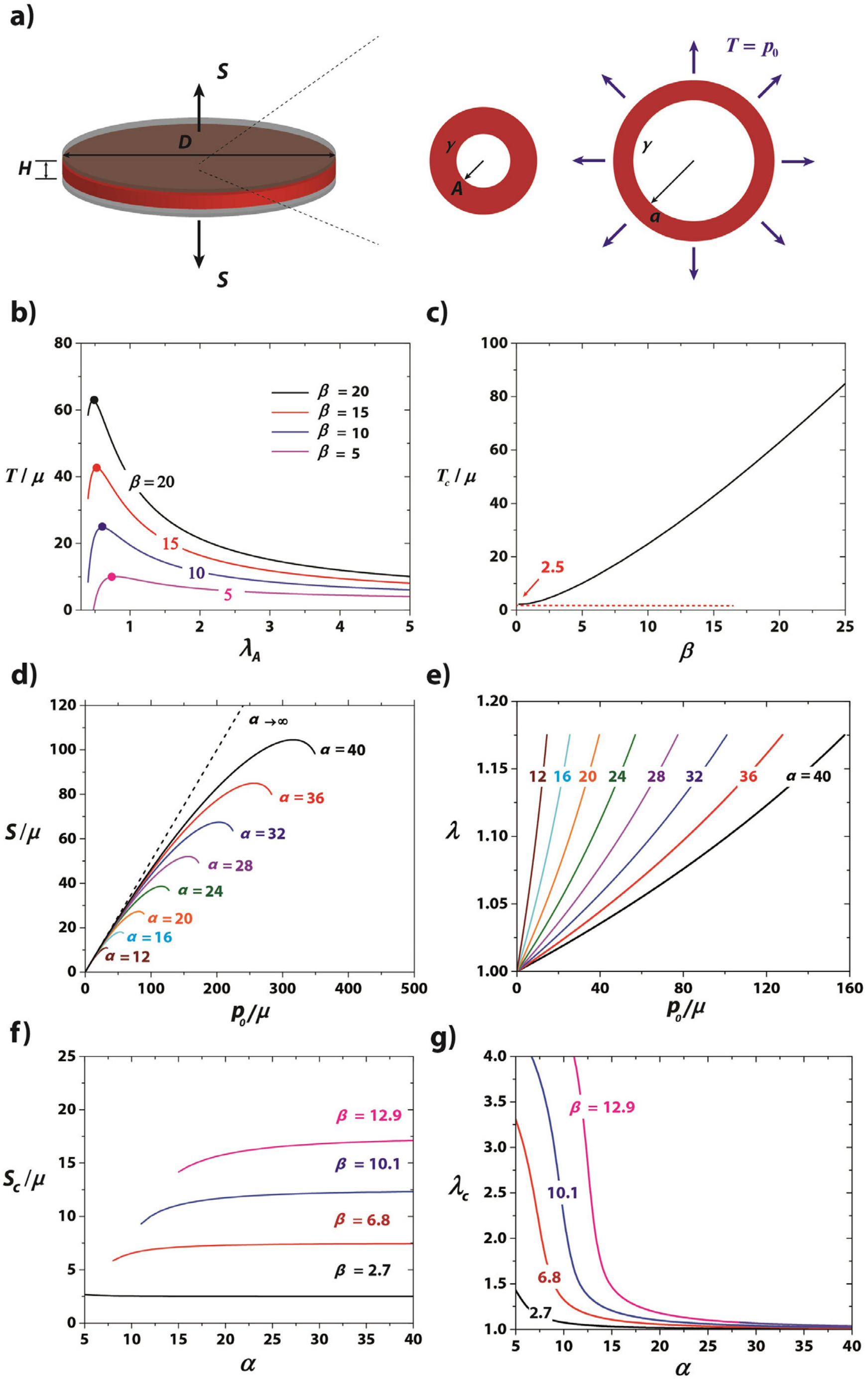

Fig. 7. Theoretical results on the critical points for cavitation instability. a) Schematic of the growth of pre-existing cavity within a cylindrical sample. b) Applied hydrostatic traction T/μ on the spherical shell versus the expansion ratio λ_A of pre-existing cavity for the material with various β. c) Critical hydrostatic traction T_c/μ for the material with various β. d) Theoretically calculated applied nominal stress S/μ versus hydrostatic pressure p_0/μ at the center of the sample. Dash line denotes the solution from theory with small strain assumption when $\alpha \to \infty$. e) Theoretically calculated stretch λ versus hydrostatic pressure p_0/μ at the center of the sample. f) Critical applied nominal stress S_c/μ for cavitation instability in samples with various α and β. g) Critical applied nominal stretch λ_c/μ for cavitation instability in samples with various α and β.

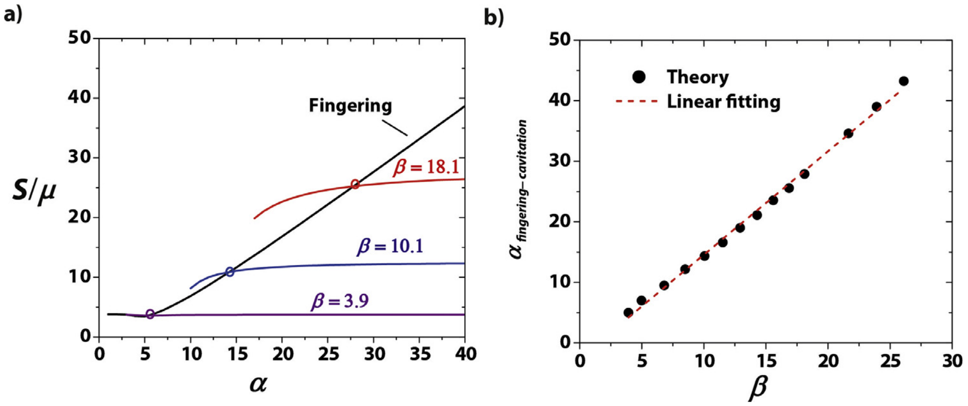

Fig. 8. Theoretical results on the transition between fingering instability and cavitation instability. a) Critical applied nominal stress for fingering stability and cavitation instability with various dimensionless capillary number β. b) Theoretical calculation of the critical transition aspect ratio $\alpha_{fingering-cavitation}$. Dashed line represents the linear fitting curve from the theoretical calculation.

6.1. Monotonic vs. non-monotonic stress–stretch relations

For the samples with small aspect ratios (e.g. $\alpha = 1$), the middle portion of the layer elongates uniformly and the constrained fringe portions deform non-uniformly into a V shape, prior to instability. Since the middle portion of the layer is almost uniformly elongated under high applied stretches (e.g. $\lambda = 1.5$, 2), the driving force for the formation of any instability in the middle portion of the layer in the sample, is limited. Instead, as the soft elastic layer is further stretched to a critical point (i.e. $\lambda_c = 4.0$ in experiment and $\lambda_c = 3.9$ in simulation), the exposed surface of the fringe portions becomes unstable—beginning to undulate periodically. The applied stress–stretch curves corresponding to fringe instability (e.g. α =2, 3, 4, 5) are all shown to be monotonic from both experiment and simulation in Fig. 9c, indicating that fringe instability is a local instability mode. The critical applied nominal stress for the onset of fringe instability with various aspect ratios is equal to 3.8 times shear modulus of the layer (see Fig. 9c and Fig. 11), which is consistent with the layers with rectangular shape (Lin et al., 2016). With the increase of aspect ratio of the layer ($\alpha > 5$), fingering instability initiates at the middle plane of the layer. As shown from the experimental and simulation results in Fig. 10a, the layer with aspect ratio $\alpha = 12$ deforms as the meniscus shape at the exposed surface at the stretch of $\lambda = 1.1$. As the stretch reaches $\lambda_c = 1.3$, undulation forms at the exposed surface and the amplitude of the fingers increases gradually with the further increase of the applied load. Different from fringe instability, the applied nominal stress–stretch curves are shown to be non-monotonic (see Fig. 10b and d). In addition, the critical applied stress increases with the increase of aspect ratio α shown in Fig. 11.

6.2. Type I fingering vs. Type II fingering

While the applied stress–stretch relations in samples subjected to fingering instability are non-monotonic, the peak stress (S_p) can exactly correspond to or slightly fall behind the critical point (S_c) for the onset of fingering instability. As shown in Fig. 10a and b for the sample with moderate aspect ratio $\alpha = 12$, the onset of fingering instability is exactly corresponding to the peak stress, which indicates this type of fingering instability is a global instability mode. In contrast, for the sample with large aspect ratio (e.g. $\alpha = 32$ in Fig. 10c and d), the emergence of fingering instability corresponds to an inflection point in the applied nominal stress–stretch curve and the stress keeps increasing until the layer reaches the peak stress, manifesting that this type of fingering instability is a local instability mode. To distinguish the two types of fingering instability, we term the instability as *Type I fingering instability* if the onset of the undulations corresponds to the maximum applied nominal stress; and term the instability as *Type II fingering instability* if the onset of the undulations deviates from the maximum applied nominal stress. We further performed cyclic loading for both layers and found that the stress–stretch curves at first loading and subsequent loading are consistent with each other, which manifests that both types of fingering instability are reversible and elastic response (see in Fig. 10b and d). To further visualize the evolution of the two types of fingering instabilities, we performed the corresponding numerical simulation in Abaqus/Explicit. Fig. 10a shows the formation of Type I fingering instability in the layer with $\alpha = 12$ and Fig. 10c shows the formation of Type II fingering instability in the layer with $\alpha = 32$. Different from Type I fingering instability, after the initiation of fingering undulations at the lateral surfaces, the applied nominal stress keeps increasing.

To further identify the transition between type I fingering instability and type II fingering instability, we measured both the critical applied nominal stress S_c for the onset of instability and the peak stress S_p from experimental and simulation results. As summarized in Fig. 11, for the samples with moderate aspect ratios (e.g. $5 < \alpha < 20$), the critical stress for the onset of instability exactly corresponds to the peak stress (i.e. $S_c = S_p$); while for the samples with large aspect ratios (e.g. $\alpha > 20$), the critical stress for the onset of instability is slightly lower than the peak stress (i.e. $S_c < S_p$). Here, we identify the critical transition aspect ratio between two types of fingering instability as $\alpha_{TypeI-TypeII} = 20$ from the numerical simulation.

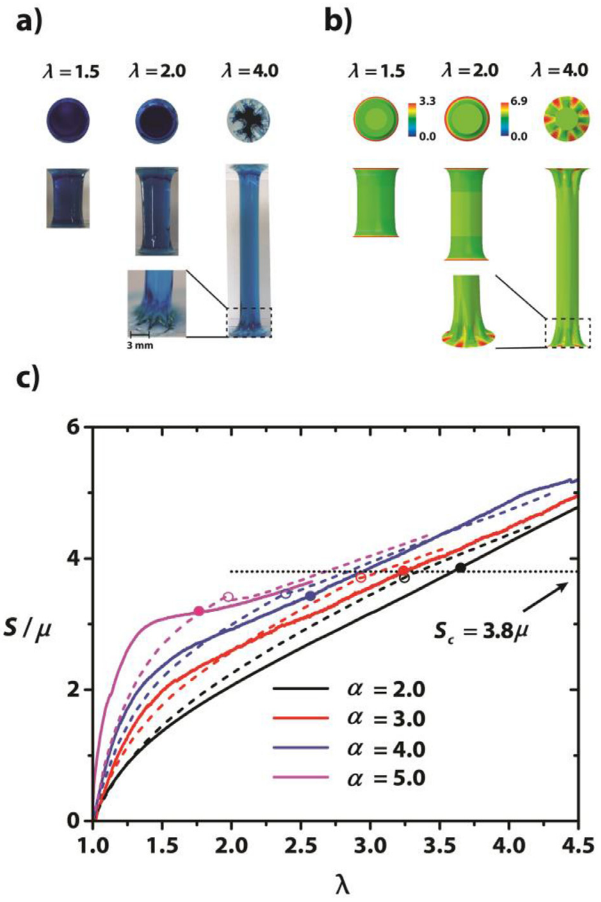

Fig. 9. Experimental and simulation results on fringe instability. a) Experimental observation and b) corresponding simulations for the formation of fringe instability for the sample with $\alpha = 1$. The color scale represents the effective true stress distribution in the deformed layer. c) Applied nominal stress versus stretch curves from experiments (solid lines) and simulations (dashed line) for the sample with $\alpha = 2, 3, 4, 5$.

7. A phase diagram for instabilities

As the applied stretch or stress on the constrained elastic layer reaches a critical value, a mode of mechanical instability sets in the layer. While the selection of fringe or fingering instability is governed by the geometry of the elastic layer via $\alpha = D/H$, the cavitation instability is also affected by material properties and defects of the elastic layer via $\beta = \gamma/\mu A$. Therefore, we can predict the occurrence of any mode of instability using a phase diagram with two control parameters: $\alpha = D/H$ and $\beta = \gamma/\mu A$.

In Section 4 and Section 5.2, we have illustrated the transition from fringe instability to fingering instability as $\alpha_{fringe-fingering} = 5$ from simulation and $\alpha_{fringe-fingering} = 4.9$ from theory. In Section 5.3, we identify the transition from fingering instability to cavitation instability as $\alpha_{fingering-cavitation} = 1.7\beta - 2.5$ for the samples with aspect ratios $\alpha > 5$. In Section 6, we identify the transition aspect ratio from Type I fingering instability to Type II as $\alpha_{TypeI-TypeII} = 20$ from numerical calculation.

With the identified $\alpha_{fringe-fingering}$, $\alpha_{fingering-cavitation}$ and $\alpha_{TypeI-TypeII}$. we construct the phase diagram in the plot of aspect ratio α and dimensionless capillary numberβ shown in Fig. 12. The solid lines in Fig. 12 are from theory and simulations. To illustrate the phase diagram, we qualitatively discusses three representative cases for the initial occurrence mode of the samples with wide range of β. For the sample with small dimensionless capillary number β(e.g. $\beta = 3.9$ in Fig. 8a and Fig. 12), fringe instability emerges at the exposed free surfaces of the sample with small aspect ratio (i.e. $\alpha < 5$). As the increase of α, cavitation instability within the sample forms prior to the formation of fingering instability. Both Type I and Type II fingering instabilities are suppressed in this case, which is commonly observed for rubber-like samples. If β is moderate large (e.g. $\beta = 10.1$ in Fig. 8a and Fig. 12), the sample exhibits fringe instability if aspect ratio is small (e.g. $\alpha < 5$), Type I fingering instability if aspect ratio is moderate large (i.e. $5 < \alpha < 14$), and cavitation instability within the sample if aspect ratio is extremely large (i.e. $\alpha > 14$). In this case, Type II fingering instability is suppressed. If β is sufficient high (e.g.

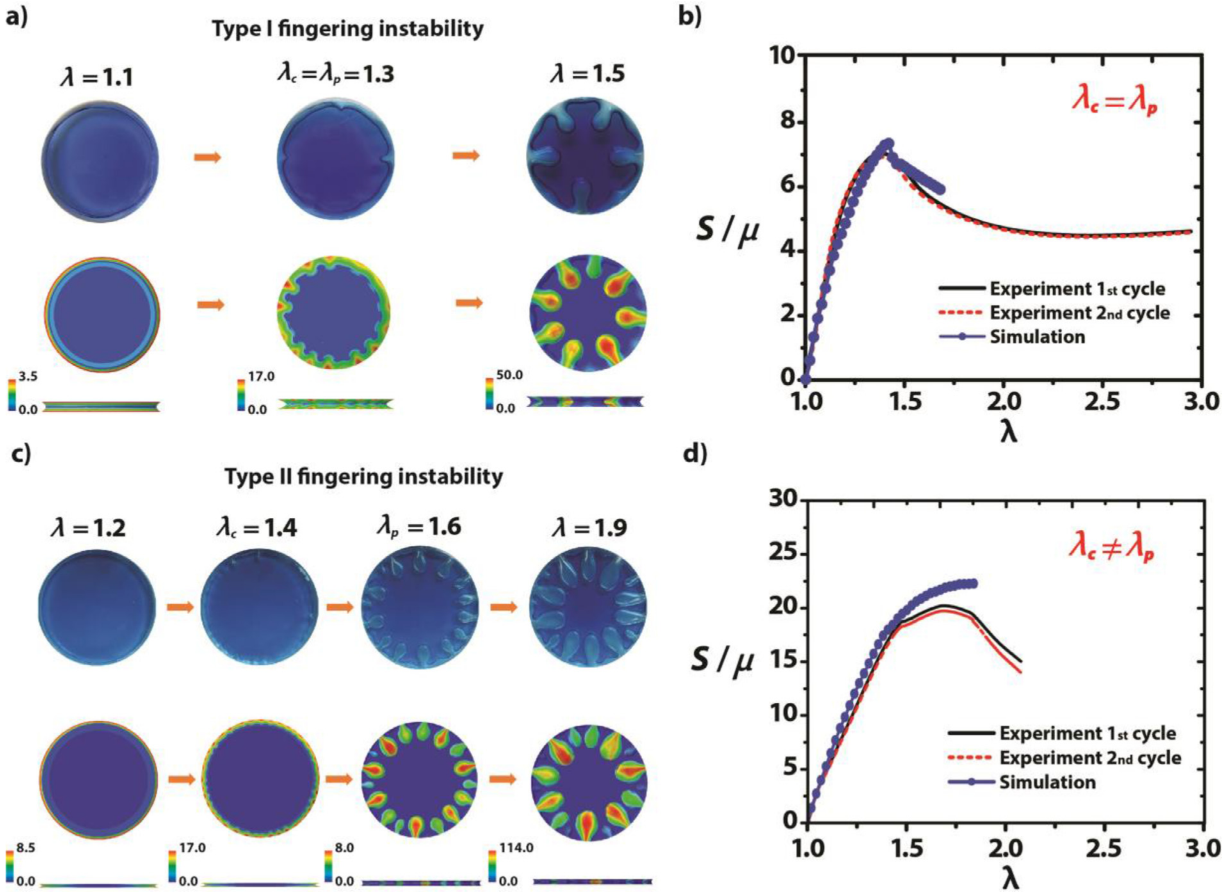

Fig. 10. Experimental and simulation results on fingering instability. a) Experimental observation and corresponding simulations for the formation of Type I fingering instability for the sample with $\alpha = 12$. b) Applied nominal stress versus stretch curves from experiments and simulations for the sample with $\alpha = 12$. c) Experimental observation and corresponding simulations for the formation of Type II fingering instability for the sample with $\alpha = 32$. d) Applied nominal stress versus stretch curves from experiments and simulations for the sample with $\alpha = 32$. Here, the bulk modulus in simulation is set as $K = 200\mu$ to match well with the experimental results, which means the sample we used is not ideally incompressible. The color scale represents the effective true stress distribution in the deformed layer.

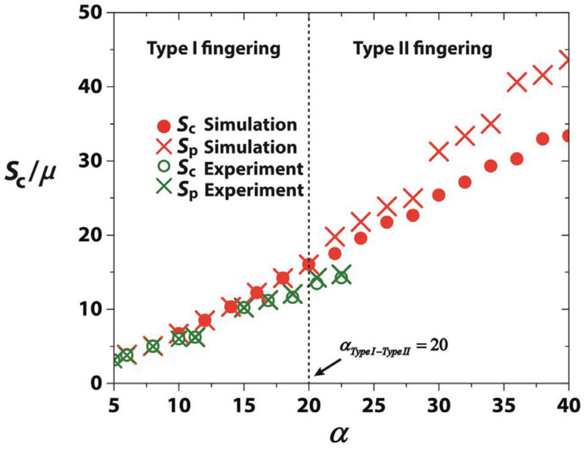

Fig. 11. Experimental and simulation results on the critical stress S_c and the peak stress S_p to identify the transition between Type I fingering instability and Type II fingering instability. When $\alpha > 20$, the critical stress for the onset of fingering instability deviates from the maximum peak stress, where Type II fingering instability sets in.

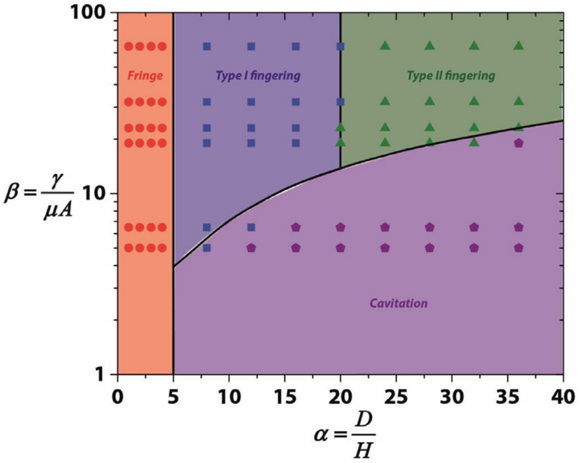

Fig. 12. Phase diagram for the initial occurrence mode of mechanical instabilities. The lines are from theory and simulation, and the dots are from experiments. Red circular dots denote the occurrence of fringe instability, blue square dots denote the occurrence of Type I fingering instability, green triangular dots denote the occurrence of Type II fingering instability and purple pentagon dots denote the occurrence of cavitation instability. (For interpretation of the references to colour in this figure legend, the reader is referred to the web version of this article.)

$\beta = 18.1$ in Fig. 8a and Fig. 12), all modes of mechanical instabilities including fringe instability, Type I fingering instability, Type II fingering instability and cavitation instability can be observed across a wide range of aspect ratios α.

The phase diagram is also validated by experiments. We chose materials with six constituents with controlled critical defect size of $A = 1\,\mu\text{m}$, surface tension $\gamma = 0.07\text{N/m}$ while varying the shear modulus μ (see details in Fig. 2). For each constituent, samples were measured across wide range of aspect ratios to investigate the initial mode of mechanical instabilities. The experimental data matches relatively well compared with the theoretical predication of the phase diagram in Fig. 12.

8. Coexistence and interactions of instabilities

From our experiments and simulations, we find that cavitation instability can coexist with fingering instability and their interactions can affect each other. We will discuss two scenarios on coexistence and interactions of cavitation and fingering instabilities: cavitation instability occurs prior to the formation of fingering instability; fingering instability forms prior to the nucleation of cavitation instability.

As shown in Fig. 13a, we show the evolution of a sample under tension from top view with aspect ratio of $\alpha = 20$ and dimensionless capillary number of $\beta \approx 7$ ($\gamma \approx 0.07\ \text{N/m}^2$, $\mu \approx 10\,\text{kPa}$ and $A \approx 1\,\mu\text{m}$). At small deformation, the applied nominal stress increases linearly with uniform shrinkage of the sample (see Fig. 13b). When the applied nominal stress reaches $\sim 60\,\text{kPa}$, a cavity nucleates suddenly in the sample and more and more cavities nucleates within the sample with the further increase of load. When the applied nominal stress reaches the maximum stress $\sim$105 kPa, the exposed meniscus becomes unstable and form periodic undulated patterns, demonstrating the coexistence of cavitation instability within the sample and fingering instability at the exposed meniscus. As the sample is further loaded, the growth of fingering tends to suppress the growth of cavitation within the sample. The coexistence of cavitation instability and fingering instability can be interpreted as follows. As shown in Fig. 13c, since the critical applied nominal stress for the onset of cavitation instability is smaller than that of the initiation of fingering instability, the onset of cavitation instability occurs first, corresponding to a negligible kink in the applied nominal stress–stretch curve (shown in Fig. 13b). The further increase of the applied load can serve as an additional driving force to initiate the fingering instability at the exposed lateral surface.

Likewise, we demonstrate another example with the sample of aspect ratio $\alpha = 28$ and dimensionless number of $\beta \approx 35$ ($\gamma \approx 0.07\ \text{N/m}^2$, $\mu \approx 2\,\text{kPa}$ and $A \approx 1\,\mu\text{m}$), in which fingering instability forms first at the exposed surface and a cavity nucleates within the sample thereafter. As shown in Fig. 13d and e, when the applied nominal stress reaches $\sim 40\,\text{kPa}$, the exposed meniscus undulated, showing fingering instability. Thereafter, the amplitude of the fingers increases gradually and a cavity nucleates within the sample when the applied nominal stress reaches $\sim$43 kPa. As the further increase of the applied load, both fingers at the exposed surfaces and the cavity within the sample grow by size gradually. As theoretical interpretation shown in Fig. 13f, the critical applied nominal stress for the onset of fingering instability is smaller than that of the initiation of cavitation instability, fingering instability forms first. Since the fingering instability in this sample ($\alpha = 24$) is Type II fingering instability, the applied nominal stress keeps increasing and gives a further driving force for the initiation of the cavitation instability.

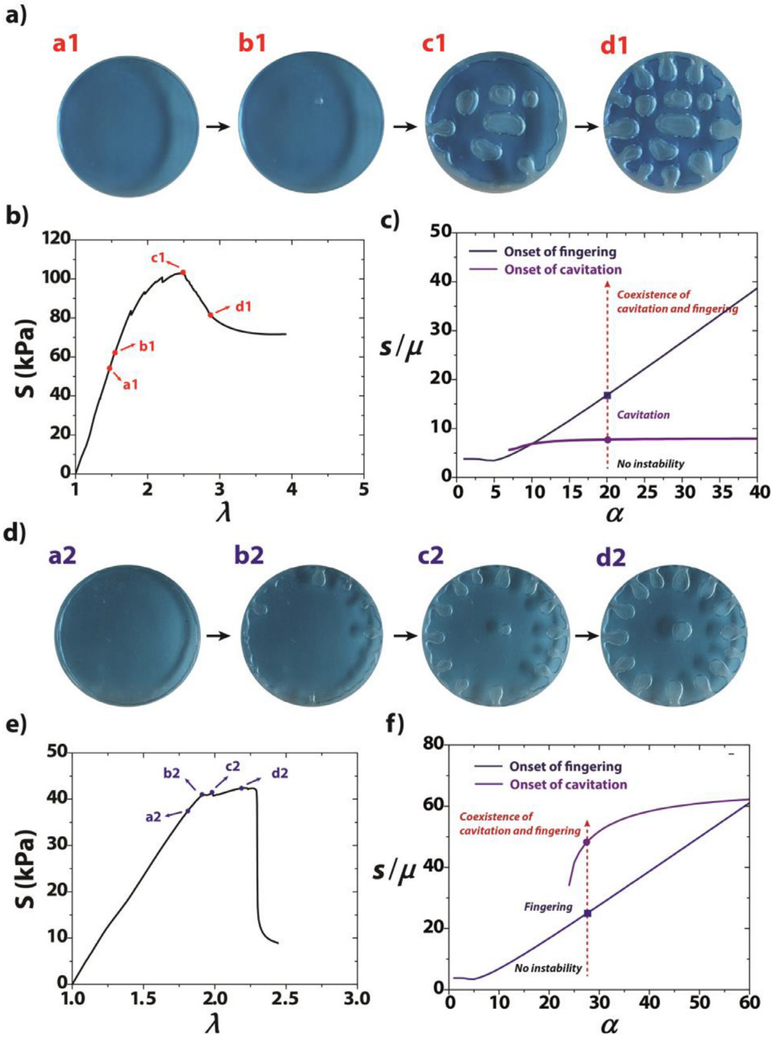

Fig. 13. Coexistence of cavitation instability and fingering instability. a), b) and c) A cavity forms suddenly within the sample, and then the applied nominal stress keeps increasing up to the maximum point which corresponds to the initiation of fingering instability at the exposed surface. The sample has an aspect ratio $\alpha = 20$ (i.e. $D = 40$ mm and $H = 2$mm) and dimensionless number of $\beta \approx 7$ ($\gamma \approx 0.07$ N/m^2, $\mu \approx 10$ kPa and $A \approx 1$ μm). d), e) and f) Type II fingering forms first at the exposed surface and a cavity forms suddenly within the sample with the further increase of the applied nominal stress, which exhibits the coexistence of Type II fingering instability and cavitation instability. The sample has an aspect ratio $\alpha = 28$ (i.e. $D = 56$ mm and $H = 2$mm) and dimensionless number of $\beta \approx 35$ ($\gamma \approx 0.07$ N/m^2, $\mu \approx 2$ kPa and $A \approx 1$ μm). The stretch rate of both experiments is 0.016 s^{-1}.

9. Concluding remarks

In this paper, we perform a systematic study on the formation, transition, interaction and co-existence of mechanical instabilities in confined elastic layers under tension through combined experimental, simulation and theoretical analysis. A phase diagram is calculated to quantitatively predict the occurrence of any mode of instability. The main conclusions are summarized as follows:

- Both fringe instability and fingering instability feature the undulation at the exposed surface. The main differences between the two instabilities are twofold. First, fringe instability initiates at the fringe portion while fingering instability forms at exact the middle plane of the layer; the stress–stretch response of the sample with fringe instability is monotonic while that of the sample with fingering instability is non-monotonic. There exists a critical transition aspect ratio between fringe and cavitation, which we identify as $\alpha_{fringe-fingering} = 5$ from simulation and $\alpha_{fringe-fingering} = 4.9$ from theory.
- For fingering instability, the point of the peak stress can exactly correspond to or slightly fall behind the critical point for the onset of fingering instability, which is corresponding to Type I fingering instability and Type II fingering instability, respectively. We identify the critical transition aspect ratio between Type I fingering and Type II fingering as $\alpha_{TypeI-TypeII} = 20$ from simulation.

- The initial occurrence mode of instability can be tuned by two dimensionless numbers: aspect ratio α and dimensionless capillary number β. For a material with controlled capillary number β, there exists a critical transition aspect ratio between fingering instability and cavitation instability, can be approximately identified as $\alpha_{fingering-cavitation} = 1.7\beta - 2.5$.
- The cavitation instability can coexist with fingering instability and interact with each other.

The systematic study on various mechanical instabilities in this paper can serve as a foundation on predicting the mechanical responses in confined elastic layers and thereafter facilitate to enhance the mechanical performance and prevent failures or ruptures. In addition to the significance in mechanical design, the tunable mode of mechanical instability can have the potential to tune the functional responses such as light transmission, electrical conductivity and acoustic transmission through mechanical stimuli.

Acknowledgments

The authors thank Professor Lallit Anand at MIT for helpful comments on the manuscript. This work is supported by ONR (No. N00014-14-1-0619), MIT Institute for Soldier Nanotechnologies and NSF (no. CMMI-1253495).

Appendix A. Detailed Derivation of the Theory in Section 5

A.1. Large deformation field in cylindrical layer under tension

We set the center of the sample as the origin point of the coordinate. We assume that the separable form is applicable to the displacement along radius direction. Therefore, the displacement field can be approximated as a 2D field, namely

$$u_R(\bar{R},\bar{Z}) = \bar{R}u_1(\bar{Z}), \tag{A1}$$

$$u_Z(\bar{Z}) = u_2(\bar{Z}), \tag{A2}$$

with $\bar{R} = \frac{R}{D/2}$, $\bar{Z} = \frac{Z}{H/2}$. Applying the displacement fields, we can further express the deformation gradient of the layer through $\mathbf{F} = \nabla\mathbf{u} + \mathbf{1}$ as:

$$\mathbf{F} = \begin{bmatrix} \lambda_{rR} & 0 & \gamma_{rZ} \\ 0 & \lambda_{\theta\Theta} & 0 \\ 0 & 0 & \lambda_{zZ} \end{bmatrix}, \tag{A3}$$

with $\lambda_{rR} = 1 + \frac{1}{D/2}u_1$,$\lambda_{\theta\Theta} = 1 + \frac{1}{D/2}u_1$, $\lambda_{zZ} = 1 + \frac{1}{H/2}\frac{du_2}{d\bar{Z}}$ and $\gamma_{rZ} = \frac{\bar{R}}{H/2}\frac{du_1}{d\bar{Z}}$. The incompressibility of the elastic layer enforces the conservation of volume, which reads as:

$$\lambda_{rR}\lambda_{\theta\Theta}\lambda_{zZ} = 1. \tag{A4}$$

We further take the elastic layer as an incompressible neo-Hookean material with strain energy density function $\psi = \frac{\mu}{2}[\mathrm{tr}(\mathbf{F}^{\mathrm{T}}\mathbf{F}) - 3]$. Therefore, the nominal stress tensor $\mathbf{S}$ is expressed through $\mathbf{S} = \mu\mathbf{F} - p^{*}\mathbf{F}^{-\mathrm{T}}$ and the Cauchy stress tensor is expressed through $\boldsymbol{\sigma} = \mathbf{S}\mathbf{F}^{\mathrm{T}}$, namely:

$$\mathbf{S}/\mu = \begin{pmatrix} \lambda_{rR} - \bar{p}/\lambda_{rR} & 0 & \gamma_{rZ} \\ 0 & \lambda_{\theta\Theta} - \bar{p}/\lambda_{\theta\Theta} & 0 \\ \lambda_{\theta\Theta}\gamma_{rZ}\bar{p} & 0 & \lambda_{zZ} - \bar{p}/\lambda_{zZ} \end{pmatrix}, \tag{A5a}$$

$$\boldsymbol{\sigma}/\mu = \begin{pmatrix} \lambda_{rR}^2 - \bar{p} + \gamma_{rZ}^2 & 0 & \gamma_{rZ}\lambda_{zZ} \\ 0 & \lambda_{\theta\Theta}^2 - \bar{p} & 0 \\ \gamma_{rZ}\lambda_{zZ} & 0 & \lambda_{zZ}^2 - \bar{p} \end{pmatrix}, \tag{A5b}$$

where p^{*} is the Lagrange Multiplier to enforce the incompressibility and $\bar{p} = p^{*}/\mu$ is the corresponding dimensionless form. The equilibrium equation reads Div $\mathbf{S}$=$\mathbf{0}$. Since the equilibrium equation along hoop direction will be satisfied automatically, then the equations along radius direction and axial direction are

$$-\frac{1}{\lambda_{rR}}\frac{\partial\bar{p}}{\partial\bar{R}} + \alpha\frac{\partial\gamma_{rZ}}{\partial\bar{Z}} = 0, \tag{A6}$$

$$\lambda_{rR}\frac{\partial(\gamma_{rZ}\bar{p})}{\partial\bar{R}} + \frac{\lambda_{rR}\gamma_{rZ}\bar{p}}{\bar{R}} + \alpha\frac{\partial(\lambda_{zZ} - \bar{p}/\lambda_{zZ})}{\partial\bar{Z}} = 0, \tag{A7}$$

with $\alpha = D/H$. Since the highest order of $\bar{R}$ in γ_{rZ} is first order and in order to satisfy the equilibrium equation Eq. (A6), $\bar{p}$ is a function of $\bar{R}^2$ and should be in the form as:

$$\bar{p}\left(\bar{R},\bar{Z}\right) = q_0\left(\bar{Z}\right) + \left(\bar{R}^2 - 1\right)q_1\left(\bar{Z}\right). \tag{A8}$$

By inserting Eq. (A8) into Eq. (A6) and using the relation of λ_{rR} and γ_{rZ} in Eq. (A3), we can attain an ODE with respect to $\bar{Z}$, reading as:

$$\alpha^2 \lambda''_{rR} = \frac{2q_1}{\lambda_{rR}}. \tag{A9}$$

By inserting Eq. (A8) into Eq. (A7) and using the incompressibility constraint Eq. (A4), we can attain another ODE:

$$\lambda_{rR}\left(2\lambda'_{rR} q_1 - \lambda_{rR} q'_1\right)\bar{R}^2 + \left[\lambda'_{zZ} - \lambda^2_{rR}\left(q'_0 - q'_1\right)\right] = 0. \tag{A10}$$

In order to satisfy Eq. (A10) for all the value of $\bar{R} \in [0, 1]$, we can further attain the following two ODEs:

$$2q_1 \lambda'_{rR} = \lambda_{rR} q'_1, \tag{A11}$$

$$\lambda'_{zZ} = \lambda^2_{rR}(q'_0 - q'_1). \tag{A12}$$

The combination of Eq. (A9) and Eq. (A11) results in one governing equation with respect to λ_{rR}, reading as:

$$\lambda''_{rR} = \pm\kappa^2 \lambda_{rR}, \tag{A13}$$

with $q_1 = \pm\frac{1}{2}\kappa^2\alpha^2\lambda^2_{rR}$, which is corresponding to two cases:

a) For case $\lambda''_{rR} = -\kappa^2\lambda_{rR}$, the general solution of Eq. (A13) is $\lambda_{rR} = C_1\cos(\kappa\bar{Z}) + C_2\sin(\kappa\bar{Z})$ where C_1 and C_2 are two constants to be determined by boundary conditions. By imposing the boundary conditions: $du_1/d\bar{Z}|_{\bar{Z}=0} = 0$, $u_1(\bar{Z} = \pm 1) = 0$, the specific function $u_1(\bar{Z})$ can be identified as:

$$u_1(\bar{Z}) = \frac{D}{2}\left(\frac{\cos(\kappa\bar{Z})}{\cos(\kappa)} - 1\right). \tag{A14a}$$

Further combining the condition of volume conservation in Eq. (A4) and boundary condition of $u_2(\bar{Z} = 0) = 0$, the specific function $u_2(\bar{Z})$ can be calculated through $u_2 = \frac{H}{2}\int_0^{\bar{Z}}\left(\frac{\cos^2\kappa}{\cos^2(\kappa\xi)} - 1\right)d\xi$, namely,

$$u_2(\bar{Z}) = \frac{H}{2}\left(\frac{\sin(2\kappa)}{2\kappa}\frac{\tan(\kappa\bar{Z})}{\tan(\kappa)} - \bar{Z}\right). \tag{A15a}$$

The deformation field in constrained elastic layer under tension can be fully specified by functions $u_1(\bar{Z})$ and $u_2(\bar{Z})$, expressed in Eq. (A14a) and Eq. (A15a), where κ is an internal loading parameter which is correlated with the applied stretch by $\lambda = \frac{u_2(\bar{Z}=1)}{H/2} + 1$, namely, $\lambda = \frac{\sin(2\kappa)}{2\kappa}$. For any $\kappa \in [0, \pi/2)$, we have $0 < \lambda \le 1$ for this case, which is corresponding to compression.

b) For case $\lambda''_{rR} = \kappa^2\lambda_{rR}$, the general solution of Eq. (A13) is $\lambda_{rR} = C_1\cosh(\kappa\bar{Z}) + C_2\sinh(\kappa\bar{Z})$, where C_1 and C_2 are two constants to be determined by boundary conditions. By imposing the boundary conditions: $du_1/d\bar{Z}|_{\bar{Z}=0} = 0$, $u_1(\bar{Z} = \pm 1) = 0$, the specific function $u_1(\bar{Z})$ can be identified as:

$$u_1(\bar{Z}) = \frac{D}{2}\left(\frac{\cosh(\kappa\bar{Z})}{\cosh(\kappa)} - 1\right). \tag{A14b}$$

Further combining the condition of volume conservation in Eq. (A4) and boundary condition of $u_2(\bar{Z} = 0) = 0$, the specific function $u_2(\bar{Z})$ can be calculated through $u_2 = \frac{H}{2}\int_0^{\bar{Z}}\left(\frac{\cosh^2\kappa}{\cosh^2(\kappa\xi)} - 1\right)d\xi$, namely,

$$u_2(\bar{Z}) = \frac{H}{2}\left(\frac{\sinh(2\kappa)}{2\kappa}\frac{\tanh(\kappa\bar{Z})}{\tanh(\kappa)} - \bar{Z}\right). \tag{A15b}$$

The deformation field in constrained elastic layer under tension can be fully specified by functions $u_1(\bar{Z})$ and $u_2(\bar{Z})$, expressed in Eq. (A14b) and Eq. (A15b), where κ is an internal loading parameter which is correlated with the applied stretch by $\lambda = \frac{u_2(\bar{Z}=1)}{H/2} + 1$, namely, $\lambda = \frac{\sinh(2\kappa)}{2\kappa}$. For any $\kappa \ge 0$, we have $\lambda \ge 1$ for this case, which is corresponding to tension.

Since we are mainly interested in the tension case in this paper, we proceed using the conclusions in case (b).

To identify the dimensionless scalar pressure $\bar{p}$, we further attain the expression of $q_0(\bar{Z})$ from the integration of Eq. (A12), reading as:

$$q_0 = \frac{\alpha^2}{2}\kappa^2\lambda^2_{rR} + \frac{1}{2\lambda^4_{rR}} + C_3, \tag{A16}$$

with C_3 being a constant determined by the boundary condition of free traction at $\bar{Z} = \bar{Z}_0$. Owning to the assumption that any horizontal plane in the layer at the un-deformed state remains planar upon deformation, it's impossible to satisfy the traction free boundary conditions at all $\bar{Z}$. Here, we enforce the boundary condition at $\bar{Z} = 0$, namely the traction $\mathbf{t}_R = \mathbf{S}\cdot\mathbf{e}_R$,

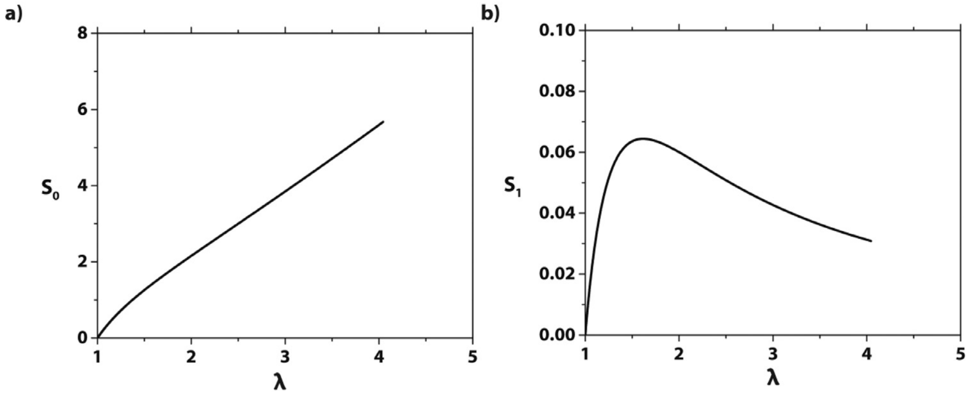

Fig. A.1. The theoretically calculated stress contains two parts: one is monotonic S_0 in a) and the other is non-monotonic S_1 in b).

shall be zero at $\bar{R}=1$. The Θ component of the traction is zero automatically and Z components of traction also be zero owing to the symmetric condition of $\gamma_{rZ}=0$ at the middle plane, and the R component reads $\mu(\lambda_{rR}-\bar{p}/\lambda_{rR})$. Therefore, constant C_3 can be identified as $\frac{1}{\cosh^2\kappa}(1-\frac{1}{2}\kappa^2\alpha^2)-\frac{1}{2}\cosh^4\kappa$ and the dimensionless scalar pressure reads as

$$\bar{p}=\frac{1}{2}\left(\frac{\cosh^4\kappa}{\cosh^4\left(\kappa\bar{Z}\right)}-\cosh^4\kappa\right)+\frac{\alpha^2\kappa^2}{2}\left(\bar{R}^2\frac{\cosh^2\left(\kappa\bar{Z}\right)}{\cosh^2\kappa}-\frac{1}{\cosh^2\kappa}\right)+\frac{1}{\cosh^2\kappa}. \tag{A17}$$

We further define the averaged nominal stress applied on the layer S as the applied force divided by the un-deformed horizontal cross-section area $\frac{\pi}{4}D^2$, which can be calculated as

$$S=\frac{4}{H\pi D^2}\cdot\frac{dW}{d\lambda}=\frac{d\tilde{W}}{d\lambda}, \tag{A18}$$

where W is the total elastic energy of the layer which can be calculated by integrating ψ over the volume of the layer: $W=2\int_0^{\frac{H}{2}}\int_0^{\frac{D}{2}}2\pi R\psi(R,Z)dRdZ$. Let $\tilde{W}=\frac{4}{H\pi D^2}W=\int_0^1\int_0^1 2\bar{R}\psi(\bar{R},\bar{Z})d\bar{R}d\bar{Z}$, by inserting the free energy $\psi=\frac{\mu}{2}[\mathrm{tr}(\mathbf{F}\mathbf{F}^{\mathrm{T}})-3]$, we can attain:

$$\tilde{W}=\frac{\mu}{2}\cdot\int_0^1\int_0^1 2\bar{R}\left(\lambda_{rR}^2+\lambda_{\theta\Theta}^2+\lambda_{zZ}^2+\gamma_{rZ}^2-3\right)d\bar{R}d\bar{Z}, \tag{A19}$$

with $\lambda_{rR}=\lambda_{\theta\Theta}=\frac{\cosh(\kappa\bar{Z})}{\cosh\kappa}$, $\lambda_{zZ}=\frac{\cosh^2\kappa}{\cosh^2(\kappa\bar{Z})}$ and $\gamma_{rZ}=\frac{\alpha\kappa}{\cosh\kappa}\sinh(\kappa\bar{Z})\bar{R}$. By integral $\tilde{W}$ over $\bar{R}$, $\tilde{W}$ can be reduced as:

$$\tilde{W}=\frac{\mu}{2}\cdot\int_0^1\left[2\frac{\cosh^2(\kappa\bar{Z})}{\cosh^2\kappa}+\frac{\cosh^4\kappa}{\cosh^4(\kappa\bar{Z})}+\frac{1}{2}\frac{\kappa^2\alpha^2}{\cosh^2\kappa}\sinh^2(\kappa\bar{Z})-3\right]d\bar{Z}. \tag{A20}$$

By integral $\tilde{W}$ over $\bar{Z}$, $\tilde{W}$can be reduced as a function with respect to a single variable κ:

$$\tilde{W}=\frac{\mu}{2}\cdot\left[\frac{\sinh\kappa\cosh\kappa+\kappa}{\kappa\cosh^2\kappa}+\frac{\sinh\kappa\cosh\kappa}{3\kappa}+\frac{2\sinh\kappa\cosh^3\kappa}{3\kappa}+\alpha^2\frac{\kappa\sinh\kappa\cosh\kappa-\kappa^2}{4\cosh^2\kappa}-3\right]. \tag{A21}$$

Combination of the Eq. (A18), Eq. (A21) and $\lambda=\frac{\sinh(2\kappa)}{2\kappa}$ gives rise to the expression of the applied nominal stress as:

$$S/\mu=S_0+\alpha^2 S_1, \tag{A22}$$

where both S_0 and S_1 are functions with respect to a single variable of loading parameter κ as:

$$\begin{aligned}S_0=&\ (6\kappa^2\sinh\kappa+3\cosh^2\kappa\sinh\kappa+\cosh^4\kappa\sinh\kappa+2\cosh^6\kappa\sinh\kappa-3\kappa\cosh\kappa\\&+\kappa\cosh^3\kappa+4\kappa\cosh^5\kappa-8\kappa\cosh^7\kappa)/\left[6\cosh^4\kappa\sinh\kappa-6\kappa\cosh^3\kappa\cosh(2\kappa)\right],\end{aligned} \tag{A23}$$

$$S_1=\left(\kappa^3\cosh\kappa-2\kappa^4\sinh\kappa-\kappa^2\cosh^2\kappa\sinh\kappa\right)/\left[8\cosh^4\kappa\sinh\kappa-8\kappa\cosh^3\kappa\cosh(2\kappa)\right] \tag{A24}$$

As shown in Fig. A.1, S_0 monotonically increases with the applied stretch while S_1 is non-monotonic with a peak point at $\kappa=0.89$ (i.e. $\lambda=1.62$).

In addition to the applied stretch λ and the applied nominal stress S we derived, the hydrostatic pressure at the center of the sample can be calculated through $p_0=\frac{1}{3}\mathrm{tr}(\boldsymbol{\sigma})|_{\bar{Z}=0,\bar{R}=0}$ with $\boldsymbol{\sigma}=\mathbf{S}\mathbf{F}^{\mathrm{T}}$ being Cauchy stress tensor. Based on Eq. (A5b), the hydrostatic pressure reads as:

$$p_0/\mu=\frac{\lambda_{rR}^2+\lambda_{\theta\Theta}^2+\lambda_{zZ}^2+\gamma_{rZ}^2}{3}-\bar{p}. \tag{A25}$$

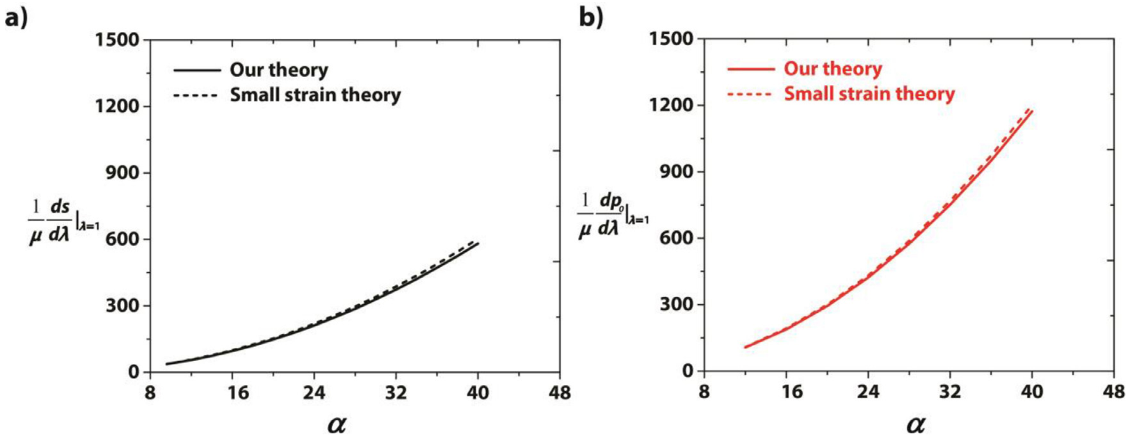

Fig. A.2. a) Comparison of $\frac{1}{\mu}\frac{ds}{d\lambda}|_{\lambda=1}$ between our result and previous result with the assumption of small deformation. b) Comparison of $\frac{1}{\mu}\frac{dp_0}{d\lambda}|_{\lambda=1}$ between our result and existing result with the assumption of small deformation.

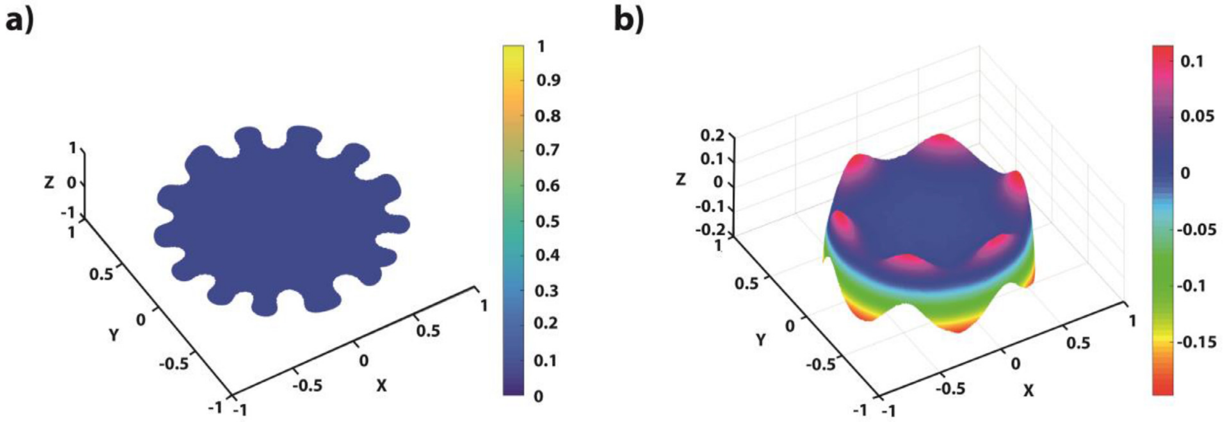

Fig. A.3. a) Undulation contour from simulation at the locus $\bar{Z}_0 = 0$ right after fingering instability for the sample with $\alpha = 8$. b) Undulation contour from simulation at the locus $\bar{Z}_0 = 0.81$ right after fringe instability for the sample with $\alpha = 4$.

Inserting $\lambda_{rR}(\bar{Z}=0)=\lambda_{\theta\Theta}(\bar{Z}=0)=\frac{1}{\cosh\kappa}$, $\lambda_{zZ}(\bar{Z}=0)=\cosh^2\kappa$, $\gamma_{rZ}(\bar{R}=0,\bar{Z}=0)=0$ and $\bar{p}(\bar{R}=0,\bar{Z}=0)=\frac{1}{\cosh^2\kappa}-\frac{\kappa^2\alpha^2}{2\cosh^2\kappa}$, one can write the hydrostatic pressure at the center of the sample as

$$p_0/\mu = \frac{\cosh^4(\kappa)}{3} - \frac{1}{3\cosh^2(\kappa)} + \frac{\kappa^2\alpha^2}{2\cosh^2(\kappa)}. \tag{A26}$$

A.2. Detailed derivation of the onset of instabilities via linear perturbation analysis

To identify the onset of fingering instability and estimating the boundary between fingering and fringe instability, we applied an infinitesimal oscillatory part to the rotational invariant part at base state solved in Section 6.1. The perturbed deformation fields read as:

$$\mathbf{x} = (\mathbf{x})^0 + \varepsilon\tilde{\mathbf{x}}, \tag{A27}$$

$$\bar{p} = (\bar{p})^0 + \varepsilon\tilde{p}, \tag{A28}$$

where the rotational invariant part is solved in Appendix. A.1, reading as:

$$(\mathbf{x})^0 = \frac{D\bar{R}}{2}\left(\frac{\cosh(\kappa\bar{Z})}{\cosh(\kappa)} - 1\right)\mathbf{e}_R + \frac{H}{2}\left(\frac{\sinh(2\kappa)}{2\kappa}\frac{\tanh(\kappa\bar{Z})}{\tanh(\kappa)} - \bar{Z}\right)\mathbf{e}_Z, \tag{A29}$$

$$(\bar{p})^0 = \frac{1}{2}\left(\frac{\cosh^4\kappa}{\cosh^4(\kappa\bar{Z})} - \cosh^4\kappa\right) + \frac{\kappa^2\alpha^2}{2}\left(\bar{R}^2\frac{\cosh^2(\kappa\bar{Z})}{\cosh^2\kappa} - \frac{1}{\cosh^2\kappa}\right) + \frac{1}{\cosh^2\kappa}. \tag{A30}$$

Both the perturbed displacement field and the perturbed Lagrange multiplier read as

$$\tilde{\mathbf{x}} = A_1(R)u_1(Z)\cos(\omega\Theta)\mathbf{e}_R + A_2(R)u_1(Z)\sin(\omega\Theta)\mathbf{e}_\Theta + A_3(R)u_2(Z)\sin(\omega\Theta)\mathbf{e}_Z, \tag{A31}$$

$$\tilde{p} = A_4(Z,R)\cos(\omega\Theta), \tag{A32}$$

where A_i $(i = 1, 2, 3, 4)$ are the amplitudes of perturbation. Therefore, the full deformation gradient may write as $\mathbf{F} = (\mathbf{F})^0 + \varepsilon\mathrm{Grad}\tilde{\mathbf{x}}$, where $(\mathbf{F})^0$ is the rotational invariant deformation gradient at base state expressed in Eq. (A3). By inserting the displacement field, the deformation gradient reads as:

$$\mathbf{F} = \begin{bmatrix} \lambda_{rR} + \varepsilon A_1' u_1 \cos(\omega\Theta) & -\varepsilon\frac{A_1\omega + A_2}{R}u_1\sin(\omega\Theta) & \gamma_{rZ} + \varepsilon A_1 u_1' \cos(\omega\Theta) \\ \varepsilon A_2' u_1 \sin(\omega\Theta) & \lambda_{\theta\Theta} + \varepsilon\frac{A_2\omega + A_1}{R}u_1\cos(\omega\Theta) & \varepsilon A_2 u_1' \sin(\omega\Theta) \\ \varepsilon A_3' u_2 \cos(\omega\Theta) & -\varepsilon\frac{A_3\omega}{R}u_2\sin(\omega\Theta) & \lambda_{zZ} + \varepsilon A_3 u_2' \cos(\omega\Theta) \end{bmatrix}. \tag{A33}$$

Here the prime is for differentiating to R and Z. The incompressibility of the elastic layer is enforced by $\det\mathbf{F} = 1$, implying till first order of ε:

$$\lambda_{rR}\lambda_{\theta\Theta}\lambda_{zZ} + \varepsilon\left(\lambda_{\theta\Theta}\lambda_{zZ}A_1'u_1 + \lambda_{rR}\lambda_{zZ}\frac{A_2\omega + A_1}{R}u_1 - \lambda_{\theta\Theta}\gamma_{rZ}A_3'u_2 + \lambda_{rR}\lambda_{\theta\Theta}A_3u_2'\right)\cos(\omega\Theta) = 1. \tag{A34}$$

By further using the conclusion from the case without perturbation we have $\lambda_{rR}\lambda_{\theta\Theta}\lambda_{zZ} = 1$ and$\lambda_{rR} = \lambda_{\theta\Theta}$, Eq. (A34) can be further reduced as:

$$\lambda_{zZ}A_1'u_1 + \lambda_{zZ}\frac{A_2\omega + A_1}{R}u_1 - \gamma_{rZ}A_3'u_2 + \lambda_{rR}A_3u_2' = 0. \tag{A35}$$

The perturbation in deformation gradient will further induce a perturbation in nominal stress which results in the nominal stress reading as $\mathbf{S}/\mu = (\mathbf{S})^0/\mu + \varepsilon\tilde{\mathbf{S}}$. The rotational invariant nominal stress $(\mathbf{S})^0/\mu = (\mathbf{F})^0 - (\bar{p})^0(\mathbf{F})^{0-\mathrm{T}}$ at base state is shown in Eq. (A7). The total stress can be calculated by inserting Eq. (A31) through $\mathbf{S}/\mu = \mathbf{F} - \bar{p}\mathbf{F}^{-\mathrm{T}}$. Therefore, the perturbed stress can be calculated as:

$$\tilde{\mathbf{S}} = \mathrm{Grad}\tilde{\mathbf{x}} + \frac{1}{\varepsilon}\left[(\bar{p})^0(\mathbf{F})^{0-\mathrm{T}} - \bar{p}\mathbf{F}^{-\mathrm{T}}\right]. \tag{A36}$$

Or alternatively, $\tilde{\mathbf{S}} = \mathrm{Grad}\tilde{\mathbf{x}} + (\bar{p})^0(\mathbf{F})^{0-\mathrm{T}}(\mathrm{Grad}\tilde{\mathbf{x}})^{-\mathrm{T}}(\mathbf{F})^{0-\mathrm{T}} - \tilde{p}(\mathbf{F})^{0-\mathrm{T}}$. By inserting Eq. (A3), Eq. (A33), Eq. (A35) and Eq. (A36), each component of the perturbed nominal stress reads as:

$$\tilde{S}_{rR} = \left[A_1'u_1 - (\bar{p})^0\left(\gamma_{rZ}A_3'u_2 - \lambda_{zZ}A_1'u_1\right) - \frac{A_4}{\lambda_{rR}}\right]\cos(\omega\Theta), \tag{A37a}$$

$$\tilde{S}_{r\Theta} = \left[-\frac{A_1\omega + A_2}{R}u_1 + (\bar{p})^0\lambda_{zZ}A_2'u_1\right]\sin(\omega\Theta), \tag{A37b}$$

$$\tilde{S}_{rZ} = \left[A_1u_1' + (\bar{p})^0\lambda_{rR}A_3'u_2\right]\cos(\omega\Theta), \tag{A37c}$$

$$\tilde{S}_{\theta R} = \left[A_2'u_1 - (\bar{p})^0\lambda_{zZ}\frac{A_1\omega + A_2}{R}u_1 + (\bar{p})^0\gamma_{rZ}\frac{A_3\omega}{R}u_2\right]\sin(\omega\Theta), \tag{A37d}$$

$$\tilde{S}_{\theta\Theta} = \left[\lambda_{rR}^2\gamma_{rZ}A_3'u_2 - \lambda_{rR}^3A_3u_2' - A_1'u_1 - (\bar{p})^0\left(\lambda_{zZ}A_1'u_1 - \gamma_{rZ}A_3'u_2 + \lambda_{rR}A_3u_2'\right) - \frac{A_4}{\lambda_{rR}}\right]\cos(\omega\Theta), \tag{A37e}$$

$$\tilde{S}_{\theta Z} = \left[A_2u_1' - (\bar{p})^0\lambda_{rR}\frac{A_3\omega}{R}u_2\right]\sin(\omega\Theta), \tag{A37f}$$

$$\tilde{S}_{zR} = \left[A_3'u_2 + \lambda_{rR}\gamma_{rZ}A_4 + (\bar{p})^0\gamma_{rZ}\left(\lambda_{rR}^2\gamma_{rZ}A_3'u_2 - \lambda_{rR}^3A_3u_2' - A_1'u_1\right) + (\bar{p})^0\lambda_{rR}A_1u_1'\right]\cos(\omega\Theta), \tag{A37g}$$

$$\tilde{S}_{z\Theta} = \left[-\frac{A_3\omega}{R}u_2 - (\bar{p})^0\gamma_{rZ}A_2'u_1 + (\bar{p})^0\lambda_{rR}A_2u_1'\right]\sin(\omega\Theta), \tag{A37h}$$

$$\tilde{S}_{zZ} = \left[A_3u_2' - \lambda_{rR}^2A_4 - (\bar{p})^0\lambda_{rR}u_1\left(A_1' + \frac{A_2\omega + A_1}{R}\right)\right]\cos(\omega\Theta). \tag{A37i}$$

A balance of the forces exerted on an element of the perturbed elastomer further leads to three equations of equilibrium through $\mathrm{Div}\,\tilde{\mathbf{S}} = 0$. The three equilibrium equations read:

$$\left\{A_1''u_1 + \left[\partial_R(\bar{p})^0\right]\left(\lambda_{zZ}A_1'u_1 - \gamma_{rZ}A_3'u_2\right) + (\bar{p})^0\left[\lambda_{zZ}A''u_1 - (\partial_R\gamma_{rZ})A_3'u_2 - \gamma_{rZ}A_3''u_2\right] - (\partial_RA_4)/\lambda_{rR}\right\}$$

$$\begin{aligned}
&+\frac{\omega}{R}\left[-\frac{A_1\omega+A_2}{R}u_1+(\bar{p})^0\lambda_{zZ}A_2'u_1\right]+A_1u_1''+\left(\partial_Z(\bar{p})^0\right)\lambda_{rR}A_3'u_2+(\bar{p})^0\lambda_{rR}'A_3'u_2+(\bar{p})^0\lambda_{rR}A_3'u_2'\\
&+\frac{1}{R}\left[2A_1'u_1+\lambda_{rR}^3A_3u_2'-\lambda_{rR}^2\gamma_{rZ}A_3'u_2+(\bar{p})^0\left(2\lambda_{zZ}A_1'u_1-2\gamma_{rZ}A_3'u_2+\lambda_{rR}A_3u_2'\right)\right]=0,
\end{aligned}\tag{A38}$$

$$\begin{aligned}
&A_2''u_1-\left[\partial_R(\bar{p})^0\right]\lambda_{zZ}\frac{A_1\omega+A_2}{R}u_1-(\bar{p})^0\lambda_{zZ}\left(\frac{A_1\omega+A_2}{R}\right)'u_1+\partial_R(\bar{p})^0\gamma_{rZ}\frac{A_3\omega}{R}u_2+(\bar{p})^0\partial_R\gamma_{rZ}\frac{A_3\omega}{R}u_2\\
&+(\bar{p})^0\gamma_{rZ}\left(\frac{A_3\omega}{R}\right)'u_2-\frac{\omega}{R}\left[\lambda_{rR}^2\gamma_{rZ}A_3'u_2-\lambda_{rR}^3A_3u_2'-A_1'u_1-(\bar{p})^0\left(\lambda_{zZ}A_1'u_1-\gamma_{rZ}A_3'u_2+\lambda_{rR}A_3u_2'\right)-\frac{A_4}{\lambda_{rR}}\right]\\
&-\left[\partial_Z(\bar{p})^0\right]\lambda_{rR}\frac{A_3\omega}{R}u_2-(\bar{p})^0\lambda_{rR}'\frac{A_3\omega}{R}u_2-(\bar{p})^0\lambda_{rR}\frac{A_3\omega}{R}u_2'+A_2u_1''\\
&+\frac{1}{R}\left[A_2'u_1-(\bar{p})^0\lambda_{zZ}\frac{A_1\omega+A_2}{R}u_1+(\bar{p})^0\gamma_{rZ}\frac{A_3\omega}{R}u_2-\frac{A_1\omega+A_2}{R}u_1+(\bar{p})^0\lambda_{zZ}A_2'u_1\right]=0,
\end{aligned}\tag{A39}$$

$$\begin{aligned}
&A_3''u_2+\lambda_R(\partial_R\gamma_{rZ})A_4+\lambda_{rR}\gamma_{rZ}(\partial_RA_4)+\left[\partial_R(\bar{p})^0\right]\left(\lambda_{rR}^2\gamma_{rZ}^2A_3'u_2-\lambda_{rR}^3\gamma_{rZ}A_3u_2'-\gamma_{rZ}A_1'u_1\right)\\
&+(\bar{p})^0\left[2\lambda_{rR}^2\gamma_{rZ}(\partial_R\gamma_{rZ})A_3'u_2+\lambda_{rR}^2\gamma_{rZ}^2A_3''u_2-\lambda_{rR}^3(\partial_R\gamma_{rZ})A_3u_2'-\lambda_{rR}^3\gamma_{rZ}A_3'u_2'-(\partial_R\gamma_{rZ})A_1'u_1-\gamma_{rZ}A_1''u_1\right]\\
&+\left[\partial_R(\bar{p})^0\right]\lambda_{rR}A_1u_1'+(\bar{p})^0\lambda_{rR}A_1'u_1'+\frac{\omega}{R}\left[-\frac{A_3\omega}{R}u_2-(\bar{p})^0\gamma_{rZ}A_2'u_1+(\bar{p})^0\lambda_{rR}A_2u_1'\right]\\
&+\frac{1}{R}\left[A_3'u_2+\lambda_{rR}\gamma_{rZ}A_4+(\bar{p})^0\gamma_{rZ}\left(\lambda_{rR}^2\gamma_{rZ}A_3'u_2-\lambda_{rR}^3A_3u_2'-A_1'u_1\right)+(\bar{p})^0\lambda_{rR}A_1u_1'\right]\\
&+A_3u_2''-2\lambda_{rR}\lambda_{rR}'A_4-\lambda_{rR}^2(\partial_ZA_4)-\left[\partial_Z(\bar{p})^0\right]\lambda_{rR}u_1\left(A_1'+\frac{A_2\omega+A_1}{R}\right)\\
&(\bar{p})^0\lambda_{rR}'\left(A_1'+\frac{A_2\omega+A_1}{R}\right)u_1-(\bar{p})^0\lambda_{rR}\left(A_1'+\frac{A_2\omega+A_1}{R}\right)u_1'=0,
\end{aligned}\tag{A40}$$

with $\lambda_{rR}=1+\frac{2}{D}u_1$, $\lambda_{\theta\Theta}=1+\frac{2}{D}u_1$ and $\gamma_{rZ}=\frac{2\bar{R}}{H}\frac{du_1}{d\bar{Z}}$, we can attain $\gamma_{rZ}=\lambda_{rR}'R=\lambda_{\theta\Theta}'R$. Taking differentiation of the incompressibility condition in Eq. (A35), we can further attain:

$$\lambda_{zZ}A_1''u_1+\lambda_{zZ}\left(\frac{A_2\omega+A_1}{R}\right)'u_1-\lambda_{rR}A_3'u_2-\gamma_{rZ}A_3''u_2+\lambda_{rR}A_3'u_2'=0,\tag{A41}$$

By imposing Eq. (A35) and Eq. (A41), all terms with $(\bar{p})^0$ in the three equilibrium equations will vanish. Thus, the three equilibrium equations can be simplified as:

$$\begin{aligned}
&\left\{A_1''u_1+\left[\partial_R(\bar{p})^0\right]\left(\lambda_{zZ}A_1'u_1-\gamma_{rZ}A_1'u_2\right)\right\}-\frac{\omega^2-1}{R^2}A_1u_1+A_1u_1''+\left[\partial_Z(\bar{p})^0\right]\lambda_{rR}A_3'u_2\\
&+\frac{1}{R}\left(3A_1'u_1+2\lambda_{rR}^3A_3u_2'-2\lambda_{rR}^2\gamma_{rZ}A_3'u_2\right)=(\partial_RA_4)/\lambda_{rR},
\end{aligned}\tag{A42}$$

$$\begin{aligned}
&\left\{A_2''u_1-\left[\partial_R(\bar{p})^0\right]\lambda_{zZ}\frac{A_1\omega+A_2}{R}u_1+\left[\partial_R(\bar{p})^0\right]\gamma_{rZ}\frac{A_3\omega}{R}u_2\right\}-\frac{\omega}{R}\left[\lambda_{rR}^2\gamma_{rZ}A_3'u_2-\lambda_{rR}^3A_3u_2'-A_1'u_1-\frac{A_4}{\lambda_{rR}}\right]\\
&-\left[\partial_Z(\bar{p})^0\right]\lambda_{rR}\frac{A_3\omega}{R}u_2+A_2u_1''+\frac{1}{R}\left[A_2'u_1-\frac{A_1\omega+A_2}{R}u_1\right]=0,
\end{aligned}\tag{A43}$$

$$\begin{aligned}
&A_3''u_2+\lambda_{rR}\gamma_{rZ}(\partial_RA_4)+\left[\partial_R(\bar{p})^0\right]\left(\lambda_{rR}^2\gamma_{rZ}^2A_3'u_2-\lambda_{rR}^3\gamma_{rZ}A_3u_2'-\gamma_{rZ}A_1'u_1+\lambda_{rR}A_1u_1'\right)+\frac{\omega}{R}\left(-\frac{A_3\omega}{R}u_2\right)\\
&+\frac{A_3'u_2}{R}+\left[A_3u_2''-\lambda_{rR}^2(\partial_ZA_4)-\partial_Z(\bar{p})^0\lambda_{rR}\left(\lambda_{rR}^2\gamma_{rZ}A_3'u_2-\lambda_{rR}^3A_3u_2'\right)\right]=0.
\end{aligned}\tag{A44}$$

Noting that all the three equilibrium equations are only required to be satisfied at $\bar{Z}=\bar{Z}_0$, where the instability initiates. For the other cross sections where $\bar{Z}\neq\bar{Z}_0$, the force balance can be satisfied automatically with $\varepsilon=0$.

For the case when fingering instability initiates, the location of the undulation is at the center plane of the sample (i.e. $\bar{Z}_0=0$). Consequently, all the terms associated with λ_{rR}', u_1' and u_2'' vanish due to the symmetric condition (e.g. $\gamma_{rZ}=0$, $\partial_Z(\bar{p})^0{}_{\bar{Z}=\bar{Z}_0}=0$). The first and third equilibrium equations can be further simplified as:

$$\left\{A_1''u_1+\left[\partial_R(\bar{p})^0\right]\lambda_{zZ}A_1'u_1\right\}-\frac{\omega^2-1}{R^2}A_1u_1+A_1u_1''+\frac{1}{R}\left(3A_1'u_1+2\lambda_{rR}^3A_3u_2'\right)=(\partial_RA_4)/\lambda_{rR},\tag{A45}$$

$$A_3''u_2 - \frac{A_3\omega^2}{R^2}u_2 + \frac{A_3'u_2}{R} = \lambda_{rR}^2\partial_Z A_4. \tag{A46}$$

For the second equilibrium equation Eq. (A43), it can be further rearranged as:

$$\begin{aligned}&-\frac{\lambda_{rR}}{\omega}\left\{RA_2''u_1 - \left[\partial_R(\bar{p})^0\right]\lambda_{zZ}(A_1\omega + A_2)u_1 + \left[\partial_R(\bar{p})^0\right]\gamma_{rZ}A_3\omega u_2\right\} + \left[\lambda_{rR}^3\gamma_{rZ}A_3'u_2 - \lambda_{rR}^4A_3u_2' - \lambda_{rR}A_1'u_1\right]\\ &+\left[\partial_Z(\bar{p})^0\right]\lambda_{rR}^2A_3u_2 - \frac{R\lambda_{rR}}{\omega}A_2u_1'' - \frac{\lambda_{rR}}{\omega}\left[A_2'u_1 - \frac{A_1\omega + A_2}{R}u_1\right] = A_4\end{aligned} \tag{A47}$$

By taking differentiation of Eq. (A47) with respect to R and neglecting any terms associated with λ_{rR}', we will attain:

$$\begin{aligned}&-\frac{\lambda_{rR}}{\omega}\left\{A_2''u_1 + RA_2^{(3)}u_1 - \left[\partial_R^2(\bar{p})^0\right]\lambda_{zZ}(A_1\omega + A_2)u_1 - \left[\partial_R(\bar{p})^0\right]\lambda_{zZ}\left(A_1'\omega + A_2'\right)u_1\right\} - \lambda_{rR}^4A_3'u_2' - \lambda_{rR}A_1''u_1\\ &-\frac{\lambda_{rR}}{\omega}A_2u_1'' - \frac{R\lambda_{rR}}{\omega}A_2'u_1'' - \frac{\lambda_{rR}}{\omega}\left[A_2''u_1 - \frac{A_1'\omega + A_2'}{R}u_1 + \frac{A_1\omega + A_2}{R^2}u_1\right] = \partial_R A_4\end{aligned} \tag{A48}$$

By taking differentiation of Eq. (A47) with respect to Z and neglecting any terms associated with λ_{rR}', we will attain:

$$\lambda_{rR}^3\lambda_{rR}''RA_3'u_2 + \left[\partial_Z^2\bar{p}_0\right]\lambda_{rR}^2A_3u_2 = \partial_Z A_4. \tag{A49}$$

The combination of Eq. (A46) and Eq. (A49) results in the second order ODE with respect to A_3, namely

$$\lambda_{rR}^3\lambda_{rR}''RA_3'u_2 + \left[\partial_Z^2\bar{p}_0\right]\lambda_{rR}^2A_3u_2 = \lambda_{zZ}A_3''u_2 + \frac{\lambda_{zZ}}{R}A_3'u_2 - \lambda_{zZ}\frac{\omega^2}{R^2}A_3u_2. \tag{A50}$$

This equation contains two solutions: one is decay solution and the other diverges as $\bar{R} \to 0$. By applying the boundary condition that $A_3'(1) = 0$, then the solution for A_3 shall be zero. However, for fringe instability, if $\alpha$is slightly smaller than the theoretical transition aspect ratio $\alpha_{fringe-fingering}$ between fingering instability and fringe instability, $A_3 \ll A_1$ and $A_3 \ll A_2$, therefore we approximate $A_3 = 0$.

By vanishing the term associated with A_3, Eq. (A45) and Eq. (A48) can be further simplified as:

$$A_1''u_1 + \left[\partial_R(\bar{p})^0\right]\lambda_{zZ}A_1'u_1 - \frac{\omega^2 - 1}{R^2}A_1u_1 + A_1u_1'' + \frac{3A_1'u_1}{R} = \frac{\partial_R A_4}{\lambda_{rR}}, \tag{A51}$$

$$\begin{aligned}&-\frac{1}{\omega}\left\{A_2''u_1 + RA_2^{(3)}u_1 - \left[\partial_R^2(\bar{p})^0\right]\lambda_{zZ}(A_1\omega + A_2)u_1 - \left[\partial_R(\bar{p})^0\right]\lambda_{zZ}\left(A_1'\omega + A_2'\right)u_1\right\} - A_1''u_1\\ &-\frac{1}{\omega}A_2u_1'' - \frac{R}{\omega}A_2'u_1'' - \frac{1}{\omega}\left[A_2''u_1 - \frac{A_1'\omega + A_2'}{R}u_1 + \frac{A_1\omega + A_2}{R^2}u_1\right] = \frac{\partial_R A_4}{\lambda_{rR}}.\end{aligned} \tag{A52}$$

Recalling the condition of incompressibility in Eq. (A35) and neglecting the terms associated with λ_{rR}' andA_3, we can attain a set of differential equations as follow:

$$A_2\omega = -\left(RA_1' + A_1\right), \tag{A53a}$$

$$A_2'\omega = -\left(2A_1' + RA_1''\right), \tag{A53b}$$

$$A_2''\omega = -\left(3A_1'' + RA_1^{(3)}\right), \tag{A53c}$$

$$A_2^{(3)}\omega = -\left(4A_1^{(3)} + RA_1^{(4)}\right). \tag{A53d}$$

The combination of Eq. (A51), Eq. (A52) and Eq. (A53) results in the fourth order ODE with respect to A_1, namely,

$$\begin{aligned}&R^4A_1^{(4)} + 6R^3A_1^{(3)} + \left\{5 - \left[\partial_R(\bar{p})^0\right]\lambda_{zZ}R + R^2u_1''/u_1 - 2\omega^2\right\}R^2A_1''\\ &-\left\{\left[\partial_R^2(\bar{p})^0\right]\lambda_{zZ}R^2 + 2\left[\partial_R(\bar{p})^0\right]R\lambda_{zZ} + 1 - 3R^2u_1''/u_1 + 2\omega^2\right\}RA_1'\\ &-\left\{R^2\left[\partial_R^2(\bar{p})^0\right]\lambda_{zZ} - 1 - R^2u_1''/u_1 - \omega^2\left(\omega^2 - 2\right) + R^2\omega^2u_1''/u_1 - R^2\left[\partial_R^2(\bar{p})^0\right]\lambda_{zZ}\omega^2\right\}A_1 = 0,\end{aligned} \tag{A54}$$

The corresponding dimensionless form reads as:

$$\begin{aligned}&\bar{R}^4A_1^{(4)} + 6\bar{R}^3A_1^{(3)} + \left\{5 - \left[\partial_{\bar{R}}(\bar{p})^0\right]\lambda_{zZ}\bar{R} + \bar{R}^2\left(\alpha^2u_1''/u_1\right) - 2\omega^2\right\}\bar{R}^2A_1''\\ &-\left\{\left[\partial_{\bar{R}}^2(\bar{p})^0\right]\lambda_{zZ}\bar{R}^2 + 2\left[\partial_{\bar{R}}(\bar{p})^0\right]\bar{R}\lambda_{zZ} + 1 - 3\bar{R}^2\left(\alpha^2u_1''/u_1\right) + 2\omega^2\right\}\bar{R}A_1'\\ &-\left\{\bar{R}^2\left[\partial_{\bar{R}}^2(\bar{p})^0\right]\lambda_{zZ} - 1 - \omega^4 + 2\omega^2 + \bar{R}^2\left(\omega^2 - 1\right)\left(\alpha^2u_1''/u_1\right) - \bar{R}^2\left[\partial_{\bar{R}}^2(\bar{p})^0\right]\lambda_{zZ}\omega^2\right\}A_1 = 0\end{aligned} \tag{A55}$$

It should be noted that the differentiations in Eq. (A55) is respecting to $\bar{R}$ or $\bar{Z}$. From Eq. (A14) and Eq. (A17) in the theory of deformation field, we attain the following relations: $[\partial_{\bar{R}}(\bar{p})^0]\lambda_{zZ} = \bar{R}\kappa^2\alpha^2$, $[\partial_{\bar{R}}^2(\bar{p})^0]\lambda_{zZ} = \kappa^2\alpha^2$and $\alpha^2 u_1''/u_1 = -\kappa^2\alpha^2\frac{\lambda_{rR}}{1-\lambda_{rR}}$. Therefore, Eq. (A55) can be further simplified as:

$$\begin{aligned}&\bar{R}^4A_1^{(4)} + 6\bar{R}^3A_1^{(3)} + \left(5 - 2\omega^2\right)\bar{R}^2A_1'' - \left(2\omega^2 + 1\right)\bar{R}A_1' + \left(\omega^2 - 1\right)^2A_1\\ &-A_h^2\bar{R}^2\left[\bar{R}^2A_1'' + 3\bar{R}A_1' - \left(\omega^2 - 1\right)A_1\right] = 0,\end{aligned} \tag{A56}$$

with $A_h = \sqrt{\frac{\kappa^2\alpha^2}{1-\lambda_{rR}}}$. By setting the boundary conditions of traction free at $\bar{R} = 1$, namely $\tilde{S}_{rR} = 0$, $\tilde{S}_{\theta R} = 0$ and $\tilde{S}_{zR} = 0$. We can attain the boundary conditions of Eq. (A56) which needs to satisfy as:

$$A_1'u_1 - (\bar{p})^0\left(\gamma_{rZ}A_3'u_2 - \lambda_{zZ}A_1'u_1\right) - \frac{A_4}{\lambda_{rR}} = 0, \tag{A57}$$

$$A_2'u_1 - (\bar{p})^0\lambda_{zZ}\frac{A_1\omega + A_2}{R}u_1 + (\bar{p})^0\gamma_{rZ}\frac{A_3\omega}{R}u_2 = 0, \tag{A58}$$

$$A_3'u_2 + \lambda_{rR}\gamma_{rZ}A_4 + (\bar{p})^0\gamma_{rZ}\left(\lambda_{rR}^2\gamma_{rZ}A_3'u_2 - \lambda_{rR}^3A_3u_2' - A_1'u_1\right) + (\bar{p})^0\lambda_{rR}A_1u_1' = 0. \tag{A59}$$

The combination of Eq. (A47) and Eq. (A57) results in the following equation in the dimensionless form as:

$$A_1^{(3)}(1) + 4A_1''(1) + \left[1 - 2\omega^2 - \zeta\omega^2 - A_h^2\right]A_1'(1) + \left[\omega^2 - 1 + \omega^2\kappa^2\alpha^2 - A_h^2\right]A_1(1) = 0, \tag{A60}$$

with $\zeta(\bar{Z}_0) = \frac{1}{2}\kappa^2\alpha^2 + \frac{1}{2}\lambda_{rR}^{-6} + C_3\lambda_{rR}^{-2}$, $C_3 = \frac{1}{\cos^2\kappa}[1 - \frac{1}{2}\kappa^2\alpha^2] - \frac{1}{2}\cos^4\kappa$.

The combination of Eq. (A53a) and Eq. (A58) results in the following equation in the dimensionless form as:

$$A_1''(1) + (2 - \zeta)A_1'(1) + \zeta\left(\omega^2 - 1\right)A_1(1) = 0. \tag{A61}$$

The third boundary condition in Eq. (A59) automatically satisfies since $A_3 \approx 0$.

In summary, the ODE for A_1 in the dimensionless form is expressed in Eq. (A56) with two boundary conditions in Eq. (A60) and Eq. (A61). To solve the forth ODE, we observe that this ODE can be separated into following two parts, both of which are in the Euler–Cauchy type:

$$\bar{R}^4A_1^{(4)} + 6\bar{R}^3A_1^{(3)} + \left(5 - 2\omega^2\right)\bar{R}^2A_1'' - \left(2\omega^2 + 1\right)\bar{R}A_1' + \left(\omega^2 - 1\right)^2A_1, \tag{A62}$$

$$\bar{R}^2A_1^{(2)} + 3\bar{R}A_1' - \left(\omega^2 - 1\right)A_1. \tag{A63}$$

If both of them goes to zero together, then the system can be solved. The corresponding characteristic functions of Eq. (A62) and Eq. (A63) are $f_1(\lambda)$ and $f_2(\lambda)$ respectively with λ is the characteristic solutions:

$$\begin{aligned}f_1(\lambda) = {}&\lambda(\lambda - 1)(\lambda - 2)(\lambda - 3) + 6\lambda(\lambda - 1)(\lambda - 2)\\ &+\left(5 - 2\omega^2\right)\lambda(\lambda - 1) - \left(2\omega^2 + 1\right)\lambda + \left(\omega^2 - 1\right)^2,\end{aligned} \tag{A64}$$

$$f_2(\lambda) = \lambda(\lambda - 1) + 3\lambda - \left(\omega^2 - 1\right). \tag{A65}$$

Owning to $f_1(-\omega - 1) = f_1(-\omega + 1) = f_1(\omega - 1) = f_1(\omega + 1) = 0$ and $f_2(-\omega - 1) = f_2(\omega - 1) = 0$, we know that both $-\omega - 1$ and $\omega - 1$ are roots of both characteristic functions. Thus, we can attain the general solution of A_1, reading as:

$$A_1\left(\bar{R}\right) = c_1\bar{R}^{\omega-1} + c_2g_2\left(\bar{R}\right)\bar{R}^{\omega+1} + c_3\bar{R}^{-\omega-1} + c_4g_4\left(\bar{R}\right)\bar{R}^{-\omega+1}, \tag{A66}$$

where $h_1(\bar{R}) = \bar{R}^{\omega-1}$, $h_2(\bar{R}) = g_2(\bar{R})\bar{R}^{\omega+1}$, $h_3(\bar{R}) = \bar{R}^{-\omega-1}$ and $h_4(\bar{R}) = g_4(\bar{R})\bar{R}^{-\omega+1}$ are four characteristic functions, and c_1, c_2, c_3 and c_4 are arbitrary pre-factors. Since we are interested in the decay solutions, and h_3 and $h_4$diverges as $\bar{R} \to 0$, thus $c_3 = c_4 = 0$.

Since c_1 and c_2 are arbitrary constants, then we can have the decay solutions in the form with $g_2 = \sum_{i=0}^{\infty}\alpha_i\bar{R}^i$ and $\alpha_0 = 1$, which indicates $h_2 = \sum_{i=0}^{\infty}\alpha_i\bar{R}^{i+\omega+1}$. Insert these back to the ODE, we can attain $\alpha_1 = 0$ and all odd terms are zero, and

$$\alpha_{i+2}f_1(i + \omega + 3) - A_h^2\alpha_if_2(i + \omega + 1) = 0; \quad i \geq 0. \tag{A67}$$

This further indicates:

$$\alpha_{2n} = A_h^{2n}\prod_{i=0}^{n-1}\frac{f_2(2i + \omega + 1)}{f_1(2i + \omega + 3)} = A_h^{2n}\prod_{i=0}^{n-1}\left[\frac{1}{4(i + 2)(\omega + i + 2)}\right] = \left(\frac{1}{2}A_h\right)^{2n}\frac{(\omega + 1)!}{(n + 1)!(n + \omega + 1)!}. \tag{A68}$$

Consequently, the decay solution reads as:

$$h_2 = (\omega + 1)!\left(\frac{2}{A_h}\right)^{\omega+1}\sum_{n=0}^{\infty}\left(\frac{1}{2}A_h\bar{R}\right)^{2n+\omega+1}\frac{1}{(n + 1)!(n + \omega + 1)!}, \tag{A69}$$

which can be further reduced to:

$$h_2 = (\omega+1)!\left(\frac{2}{A_h}\right)^{\omega+1}\left[I_\omega\left(A_h\bar{R}\right) - \frac{1}{\omega!}\left(\frac{A_h\bar{R}}{2}\right)^{\omega}\right]\left(\frac{2}{A_h\bar{R}}\right), \tag{A70}$$

with $I_\omega(\bullet)$ is the modified Bessel function of the first kind. For simplicity, we set $h_1 = \bar{R}^{\omega-1}$ and $h_2 = \frac{1}{I_\omega(A_h)} I_\omega(A_h\bar{R})\bar{R}^{-1}$, leading to the solution of A_1:

$$A_1 = c_1\bar{R}^{\omega-1} + c_2\frac{1}{I_\omega(A_h)} I_\omega\left(A_h\bar{R}\right)\bar{R}^{-1}, \tag{A71}$$

Non-trivial solution requires c_1 and c_2 cannot be zero simultaneously. Recalling the boundary condition in Eq. (A60) and Eq. (A61) and by combining these two with Eq. (A68), we can further attain

$$\frac{c_1}{c_2} = \frac{lA_h\frac{I_{\omega-1}(A_h)}{I_\omega(A_h)} - \left(A_h^2 + l\omega^2 + l\omega\right)}{l\omega(\omega-1)}, \tag{A72}$$

$$\frac{c_1}{c_2} = \frac{l\omega^2 A_h\frac{I_{\omega-1}(A_h)}{I_\omega(A_h)} - \left[l\omega^3 + l\omega^2 + \omega^2\kappa^2\alpha^2\right]}{\omega^2\kappa^2\alpha^2 - \omega A_h^2 - l\omega^3 + l\omega^2}, \tag{A73}$$

with $l = 1 + \zeta$. The existence of non-trivial solution requires Eq. (A72) and Eq. (A73) be satisfied simultaneously. After simplifying it, we have,

$$\begin{aligned}&\left(l^2\omega^3 A_h + lA_h^3 - l^2\omega A_h\right)\frac{I_{\omega-1}(A_h)}{I_\omega(A_h)} - \left(2l\omega^2 A_h^2 + 2l^2\omega^4 - 2l^2\omega^2 + A_h^4\right)\\ &+\left(2l\omega^2 + \omega A_h^2 - l\omega A_h\frac{I_{\omega-1}(A_h)}{I_\omega(A_h)}\right)\kappa^2\alpha^2 = 0.\end{aligned} \tag{A74}$$

Eq. (A74) gives the critical stretch for each mode of instability. The minimum critical stretch of a critical mode of instability ω_c results in the critical stretch λ_c of the sample with aspect ratio α. We solved Eq. (A74) numerically. The critical stretch λ_c, the critical number of instability ω_c and the critical stress S_c for the sample with different aspect ratios of α are summarized in Fig. 5.

References

Ball, J.M., 1982. Discontinuous equilibrium solutions and cavitation in nonlinear elasticity. Philos. Trans. R. Soc. Lond. A: Math. Phys. Eng. Sci. 306, 557–611.

Benjamin, M., Toumi, H., Ralphs, J., Bydder, G., Best, T., Milz, S., 2006. Where tendons and ligaments meet bone: attachment sites (‘entheses’) in relation to exercise and/or mechanical load. J. Anat. 208, 471–490.

Biggins, J.S., Saintyves, B., Wei, Z., Bouchaud, E., Mahadevan, L., 2013. Digital instability of a confined elastic meniscus. Proc. Natl. Acad. Sci. 110, 12545–12548.

Biwa, S., 2006. Cavitation in finite elasticity with surface energy effects. Int. J. Nonlinear Mech. 41, 1084–1094.

Casares, L., Vincent, R., Zalvidea, D., Campillo, N., Navajas, D., Arroyo, M., Trepat, X., 2015. Hydraulic fracture during epithelial stretching. Nat. Mater. 14, 343–351.

Cha, C., Antoniadou, E., Lee, M., Jeong, J.H., Ahmed, W.W., Saif, T.A., Boppart, S.A., Kong, H., 2013. Tailoring hydrogel adhesion to polydimethylsiloxane substrates using polysaccharide glue. Angew. Chem. Int. Ed. 52, 6949–6952.

Chakrabarti, A., Chaudhury, M.K., 2013. Direct measurement of the surface tension of a soft elastic hydrogel: exploration of elastocapillary instability in adhesion. Langmuir 29, 6926–6935.

Chaudhury, M.K., Chakrabarti, A., Ghatak, A., 2015. Adhesion-induced instabilities and pattern formation in thin films of elastomers and gels. Eur. Phys. J. E 38, 1–26.

Chung, J., Kim, K., Chaudhury, M., Sarkar, J., Sharma, A., 2006. Confinement-induced instability and adhesive failure between dissimilar thin elastic films. Eur. Phys. J. E 20, 47–53.

Chung, J.Y., Chaudhury, M.K., 2005. Soft and hard adhesion. J. Adhes. 81, 1119–1145.

Creton, C., Ciccotti, M., 2016. Fracture and adhesion of soft materials: a review. Rep. Prog. Phys. 79, 046601.

Crosby, A.J., Shull, K.R., Lakrout, H., Creton, C., 2000. Deformation and failure modes of adhesively bonded elastic layers. J. Appl. Phys. 88, 2956–2966.

Desmond, K.W., Zacchia, N.A., Waite, J.H., Valentine, M.T., 2015. Dynamics of mussel plaque detachment. Soft Matter 11, 6832–6839.

Dollhofer, J., Chiche, A., Muralidharan, V., Creton, C., Hui, C., 2004. Surface energy effects for cavity growth and nucleation in an incompressible neo-Hookean material—modeling and experiment. Int. J. Solids Struct. 41, 6111–6127.

Fond, C., 2001. Cavitation criterion for rubber materials: a review of void-growth models. J. Polym. Sci. Part B: Polym. Phys. 39, 2081–2096.

Gent, A., 1990. Cavitation in rubber: a cautionary tale. Rubber Chem. Technol. 63, 49–53.

Gent, A., Lindley, P., 1959a. The compression of bonded rubber blocks. Proc. Inst. Mech. Eng. 173, 111–122.

Gent, A., Lindley, P., 1959b. Internal rupture of bonded rubber cylinders in tension. In: Proceedings of the Royal Society of London A: Mathematical, Physical and Engineering Sciences. The Royal Society, pp. 195–205.

Ghatak, A., Chaudhury, M.K., 2003. Adhesion-induced instability patterns in thin confined elastic film. Langmuir 19, 2621–2631.

Hang-Sheng, H., Abeyaratne, R., 1992. Cavitation in elastic and elastic-plastic solids. J. Mech. Phys. Solids 40, 571–592.

Keplinger, C., Sun, J.-Y., Foo, C.C., Rothemund, P., Whitesides, G.M., Suo, Z., 2013. Stretchable, transparent, ionic conductors. Science 341, 984–987.

Kim, Y.S., Liu, M., Ishida, Y., Ebina, Y., Osada, M., Sasaki, T., Hikima, T., Takata, M., Aida, T., 2015. Thermoresponsive actuation enabled by permittivity switching in an electrostatically anisotropic hydrogel. Nat. Mater. 14, 1002–1007.

Klingbeil, W.W., Shield, R.T., 1966. Large-deformation analyses of bonded elastic mounts. Z. angew. Math. Phys. ZAMP 17, 281–305.

Kundu, S., Crosby, A.J., 2009. Cavitation and fracture behavior of polyacrylamide hydrogels. Soft Matter 5, 3963–3968.

Lefèvre, V., Ravi-Chandar, K., Lopez-Pamies, O., 2015. Cavitation in rubber: an elastic instability or a fracture phenomenon? Int. J. Fract. 192, 1–23.

Lin, S., Cao, C., Wang, Q., Gonzalez, M., Dolbow, J.E., Zhao, X., 2014a. Design of stiff, tough and stretchy hydrogel composites via nanoscale hybrid crosslinking and macroscale fiber reinforcement. Soft Matter 10, 7519–7527.

Lin, S., Cohen, T., Zhang, T., Yuk, H., Abeyaratne, R., Zhao, X., 2016. Fringe instability in constrained soft elastic layers. Soft Matter 12, 8899–8906.
Lin, S., Yuk, H., Zhang, T., Parada, G.A., Koo, H., Yu, C., Zhao, X., 2016. Stretchable hydrogel electronics and devices. Adv. Mater 28, 4497–4505.
Lin, S., Zhou, Y., Zhao, X., 2014b. Designing extremely resilient and tough hydrogels via delayed dissipation. Extreme Mech. Lett. 1, 70–75.
Lind, J.U., Busbee, T.A., Valentine, A.D., Pasqualini, F.S., Yuan, H., Yadid, M., Park, S.-J., Kotikian, A., Nesmith, A.P., Campbell, P.H., 2017. Instrumented cardiac microphysiological devices via multimaterial three-dimensional printing. Nat. Mater. 16, 303–308.
Liu, X., Tang, T.-C., Tham, E., Yuk, H., Lin, S., Lu, T.K., Zhao, X., 2017. Stretchable living materials and devices with hydrogel–elastomer hybrids hosting programmed cells. Proc. Natl. Acad. Sci. 114, 2200–2205.
Long, R., Hui, C.-Y., 2010. Effects of triaxiality on the growth of crack-like cavities in soft incompressible elastic solids. Soft Matter 6, 1238–1245.
Lopez-Pamies, O., Idiart, M.I., Nakamura, T., 2011. Cavitation in elastomeric solids: I—a defect-growth theory. J. Mech. Phys. Solids 59, 1464–1487.
Mao, Y., Lin, S., Zhao, X., Anand, L., 2017. A large deformation viscoelastic model for double-network hydrogels. J. Mech. Phys. Solids 100, 103–130.
Overvelde, J.T., Dykstra, D.M., de Rooij, R., Weaver, J., Bertoldi, K., 2016. Tensile instability in a thick elastic body. Phys. Rev. Lett. 117, 094301.
Palleau, E., Morales, D., Dickey, M.D., Velev, O.D., 2013. Reversible patterning and actuation of hydrogels by electrically assisted ionoprinting. Nat. Commun. 4, 2257.
Rose, S., Prevoteau, A., Elzière, P., Hourdet, D., Marcellan, A., Leibler, L., 2014. Nanoparticle solutions as adhesives for gels and biological tissues. Nature 505, 382–385.
Shariff, M., 1989. An analysis of non-linear deformation of bonded rubber mounts. Proc. Inst. Mech. Eng. Part C: Mech. Eng. Sci. 203, 113–119.
Shull, K.R., 2002. Contact mechanics and the adhesion of soft solids. Mater. Sci. Eng.: R: Rep. 36, 1–45.
Shull, K.R., Flanigan, C.M., Crosby, A.J., 2000. Fingering instabilities of confined elastic layers in tension. Phys. Rev. Lett. 84, 3057.
Stringfellow, R., Abeyaratne, R., 1989. Cavitation in an elastomer: comparison of theory with experiment. Mater. Sci. Eng.: A 112, 127–131.
Tupholme, G., Gover, M., 2002. Axial loading of bonded rubber blocks. J. Appl. Mech 69 (6), 836–843.
Vaccaro, E., Waite, J.H., 2001. Yield and post-yield behavior of mussel byssal thread: a self-healing biomolecular material. Biomacromolecules 2, 906–911.
Waite, J.H., Andersen, N.H., Jewhurst, S., Sun, C., 2005. Mussel adhesion: finding the tricks worth mimicking. J. Adhes. 81, 297–317.
Yang, C.H., Wang, M.X., Haider, H., Yang, J.H., Sun, J.-Y., Chen, Y.M., Zhou, J., Suo, Z., 2013. Strengthening alginate/polyacrylamide hydrogels using various multivalent cations. ACS Appl. Mater. Interf. 5, 10418–10422.
Yuk, H., Lin, S., Ma, C., Takaffoli, M., Fang, N.X., Zhao, X., 2017. Hydraulic hydrogel actuators and robots optically and sonically camouflaged in water. Nat. Commun. 8, 14230.
Yuk, H., Zhang, T., Lin, S., Parada, G.A., Zhao, X., 2016a. Tough bonding of hydrogels to diverse non-porous surfaces. Nat. Mater. 15, 190–196.
Yuk, H., Zhang, T., Parada, G.A., Liu, X., Zhao, X., 2016b. Skin-inspired hydrogel-elastomer hybrids with robust interfaces and functional microstructures. Nat. Commun. 7, 12028.
Zimberlin, J.A., Crosby, A.J., 2010. Water cavitation of hydrogels. J. Polym. Sci. Part B: Polym. Phys. 48, 1423–1427.
Zimberlin, J.A., Sanabria-DeLong, N., Tew, G.N., Crosby, A.J., 2007. Cavitation rheology for soft materials. Soft Matter 3, 763–767.